

REPORT DOCUMENTATION PAGE				Form Approved OMB No. 0704-0188	
Public reporting burden for this collection of information is estimated to average 1 hour per response, including the time for reviewing instructions, searching existing data sources, gathering and maintaining the data needed, and completing and reviewing the collection of information. Send comments regarding this burden estimate or any other aspect of this collection of information, including suggestions for reducing the burden, to Department of Defense, Washington Headquarters Services, Directorate for Information Operations and Reports (0704-0188), 1215 Jefferson Davis Highway, Suite 1204, Arlington, VA 22202-4302. Respondents should be aware that notwithstanding any other provision of law, no person shall be subject to any penalty for failing to comply with a collection of information if it does not display a currently valid OMB control number. PLEASE DO NOT RETURN YOUR FORM TO THE ABOVE ADDRESS.					
1. REPORT DATE (DD-MM-YYYY) 19-10-2004		2. REPORT TYPE Final Report		3. DATES COVERED (From – To) 1 October 2003 - 20-Oct-04	
4. TITLE AND SUBTITLE Propagation Of High-Power, Femtosecond Laser Radiation Through The Atmosphere			5a. CONTRACT NUMBER FA8655-03-D-0001, Delivery Order 0009		
			5b. GRANT NUMBER		
			5c. PROGRAM ELEMENT NUMBER		
6. AUTHOR(S) Professor Alexander Zemlyanov			5d. PROJECT NUMBER		
			5d. TASK NUMBER		
			5e. WORK UNIT NUMBER		
7. PERFORMING ORGANIZATION NAME(S) AND ADDRESS(ES) Institute of Atmospheric Optics, Siberian Branch 1 Akademicheskii Ave Tomsk 634055 Russia				8. PERFORMING ORGANIZATION REPORT NUMBER N/A	
9. SPONSORING/MONITORING AGENCY NAME(S) AND ADDRESS(ES) EOARD PSC 802 BOX 14 FPO 09499-0014				10. SPONSOR/MONITOR'S ACRONYM(S)	
				11. SPONSOR/MONITOR'S REPORT NUMBER(S) EOARD Task 03-9002	
12. DISTRIBUTION/AVAILABILITY STATEMENT Approved for public release; distribution is unlimited.					
13. SUPPLEMENTARY NOTES					
14. ABSTRACT This report results from a contract tasking Institute of Atmospheric Optics, Siberian Branch as follows: The contractor will investigate theoretically the interaction between femtosecond propagation effects and atmospheric turbulence, supercontinuum emission (spectral broadening), nonlinear scattering by atmospheric aerosols, and theoretical upper and lower limits for nonlinear propagation effects.					
15. SUBJECT TERMS EOARD, Femtosecond pulses, Atmospheric Propagation, Nonlinear Optics					
16. SECURITY CLASSIFICATION OF:			17. LIMITATION OF ABSTRACT UL	18, NUMBER OF PAGES 56	19a. NAME OF RESPONSIBLE PERSON DONALD J SMITH
a. REPORT UNCLAS	b. ABSTRACT UNCLAS	c. THIS PAGE UNCLAS			19b. TELEPHONE NUMBER <i>(Include area code)</i> +44 (0)20 7514 4953

Project technical report

Duration: October, 2003 – September 2004

CRDF grant: RP0-1390-TO-03

Project objectives:

- The theoretical study of powerful femtosecond laser pulse filamentation in the turbulent atmosphere.
- Researching the supercontinuum cone emission mechanism by numerical simulation of high-power femtosecond laser pulse propagation in the atmosphere.
- The theoretical and experimental study of the fundamental problems of scattering of a high-power femtosecond pulse in the atmosphere: nonstationary light scattering in gases and aerosols; nonlinear inelastic nonstationary light scattering by aerosols particles.

Contents

Introduction	2
1. The theoretical study of powerful femtosecond laser pulse filamentation in the turbulent atmosphere	6
2. Researching the supercontinuum cone emission mechanism by numerical simulation of high-power femtosecond laser pulse propagation in the atmosphere	10
3. The theoretical and experimental study of the fundamental problems of scattering of a high-power femtosecond pulse in the atmosphere: nonstationary light scattering in gases and aerosols; nonlinear inelastic nonstationary light scattering by aerosols particles	20
Conclusion	50
References	53

Introduction

Obvious progress achieved recently in development of new laser technologies stimulates their active use in optics of natural media. Unique properties of laser radiation allow new information on the objects under study to be obtained. A prominent example is the application of femtosecond lasers to atmospheric sensing, clearly demonstrating the increase in accuracy, sensitivity, and range of sensing. The use of broadband femtosecond radiation, as well as initiated by the radiation white supercontinuum due to filamentation, significantly extend the list of measured parameters of the environment and allow sensing of ecologically dangerous gaseous and aerosol substances.

For efficient application of high-power lasers in the environmental research, it is important to know how the high-power laser radiation propagates in the atmosphere and how one can improve properties of the radiation as a research instrument. This knowledge is also important for many other practical applications.

The use of high-power lasers in environmental research is a complex problem including both basic and applied aspects. To be noted among them are nonlinear optics of the atmosphere, problems of linear and nonlinear propagation of optical radiation in the atmosphere, adaptive optics, and laser technologies of diagnostics of natural media.

Filamentation is manifested in the localization of a significant fraction of the initial laser pulse energy within a narrow axial region [1-3]. Typically, the filaments are produced by Ti:Sapphire laser amplification systems with the central wavelength of 770-810 nm, pulse duration 50 – 200 fs and peak power up to 1-2 TW. The length of the localized structure is up to several hundred meters or even kilometers [4] with the transverse diameter of the order of $\sim 100\ \mu\text{m}$. The maximum intensity in the filament is saturated at the value $\sim 5 \cdot 10^{13}\ \text{W/cm}^2$ corresponding to the threshold intensity for the ionization of air. Such confined propagation is accompanied by the generation of a wide frequency spectrum – supercontinuum. The supercontinuum band generated by terawatt 35 fs 800 nm pulses in air extends from 0.35 to $4.5\ \mu\text{m}$ [5]. This makes possible to use filamentation phenomenon for remote sensing applications. Indeed, remote sensing of the atmosphere requires a broadband light source, the radiation of which can be delivered to the object of investigation, such as, e.g., an aerosol layer located at a certain distance from the ground surface. Extended localization of a high-power femtosecond laser pulse in air opens a new and unique way to construct such a broadband source because the forwardly directed supercontinuum, accompanying filamentation, can reach the altitudes as high as 10 km [4]. The backscattered light brings the information about the atmospheric constituents. Thus, the combination of a broadband light produced by a femtosecond pulse and the appropriate time and frequency-resolved registration system of the backscattered light provides us with a femtosecond lidar [4, 6].

The key parameter for femtosecond remote sensing is the amount of the initial pulse energy converted into a white light energy. In order to optimize this conversion efficiency, the physical origin of the supercontinuum in the course of the filamentation should be found out. The generated supercontinuum should be delivered to the specified location of interest. This location can be controlled by adjustment of the initial pulse parameters, such as chirp and initial wavefront curvature.

For the remote sensing applications it is important that the filament is stable from one laser shot to another.

However, in practice, there could be several reasons leading to the displacement of the filament starting position in both longitudinal and transverse directions. Among the reasons for these random shot-to-shot displacements there could be initial intensity and phase perturbations in the beam profile introduced by high-power laser amplification system, random angular deflections, refractive index fluctuations caused by atmospheric turbulence.

Random perturbations of the phase due to the refractive index fluctuations in turbulence are transformed into the intensity fluctuations. The latter develop into the hot spots and seed the formation of filaments. For a terawatt pulse its peak power is hundred times larger than the critical power for self-focusing in air. Therefore, random multiple filaments are formed in atmospheric turbulence. Statistical characteristics of atmospheric turbulence define the scenario of the formation and properties of a bunch of multiple filaments. Thus, the process of filament formation in terawatt femtosecond laser pulse in the atmosphere is, by definition, stochastic. Each of the multiple filaments is a source of plasma and white light. Therefore, stochastic nature of multiple filamentation might be the reason for the instability of the nonlinear fluorescence [7] as well as supercontinuum signal [4] in atmospheric lidar systems. Studying of multifilamentation in the turbulent atmosphere is of crucial importance for improving the methods of the remote sensing [4,6] and lightning discharge control [8].

In spite of almost century-long history, the problem of elastic linear scattering of optical radiation by dielectric spherical microparticles remains urgent by now. It is known that the basic principles of this theory formulated still in papers by Debye [9] and Mie [10] and then developed in Refs. 11 – 14 are concerned with diffraction of a plane monochromatic light wave at a particle under stationary conditions.

As applied to the process of elastic light scattering by a particle, the condition of stationarity means that the time of establishment of optical fields in a particle and beyond it is much shorter than the duration of the diffracting radiation pulse and, consequently, the establishment of optical fields can be considered as instantaneous. At the same time, light scattering, as any other physical process, always has nonstationary phases in its development. This circumstance is especially important in connection with promises of applying ultrashort laser pulses in aerosol optics [6]. In such time scales, the nonstationarity of the scattering process becomes comparable with the duration of a radiation pulse.

The studies of the temporal and spectral structures of the field of elastic scattering by weakly absorbing spherical particles [15] revealed the existence of free electromagnetic oscillations in dielectric spheres, whose frequencies are determined by the particle size and optical properties. If the frequency of the incident radiation coincides with the frequency of some particle eigenmode, an internal optical field is resonantly excited, and the spatiotemporal distribution of this field is completely determined by the field of the excited mode. Characteristic lifetimes τ_R of the highest-Q resonances (whispering gallery modes) in micron-sized particles usually lie in the nanosecond region [16]. Thus, if the length of the initial radiation pulse is comparable with and shorter than the time τ_R , then its scattering by a particle may have the nonstationary character.

Theoretical investigations of nonstationary light scattering are based on solutions of Maxwell's equations in their complete form with allowance for the temporal variability of the fields. A well-known approach to solution of this problem is the method of the spectral Fourier analysis [17-20]. It allows the problem on nonstationary scattering of a pulse with a spectral distribution to be reduced to scattering of a set of monochromatic Fourier harmonics. In this case, particle scattering properties are characterized by the so-called

spectral response function, which is a traditional Mie series written for all frequencies of the initial pulse spectrum. The scattered and internal fields are written in the form of the convolution integral of the pulse spectrum and the spectral response function of the particle [20]. The analytical solution of this light scattering problem was obtained only for some particular cases (optically small particles [18]), when the spectral response function has a quite simple form. Some numerical solutions of this problem that describe the behavior of the internal [18,20] and external [19] fields of the scattered wave were obtained as well.

Among various numerical methods, to be noted is the finite-difference time domain method, which is, in fact, the direct numerical solution of the nonstationary Maxwell equations [21,22]. It is worth using this method in calculations of light diffraction at objects having a complex geometry, as well as inhomogeneities in their optical properties.

In the recent years, the use of significantly nonstationary sources, such as picosecond and femtosecond lasers, for excitation of molecular fluorescence attracts considerable attention. The application of such sources in the atmosphere allows the power characteristics of the radiation and the received signal to be increased significantly without optical breakdown of the medium, which, as known, considerably restricts the range of laser radiation propagation in the nanosecond time region [16].

The phenomenon of spontaneous emission of atoms and molecules in a high-Q resonator was traditionally studied by classical and quantum electrodynamics. In these studies, the emphasis was on the problems connected with quantum characteristics of spontaneous emission of molecules into resonator modes. Macroscopic optics of emitting dipoles was studied in the papers [23-25], where the equations were derived for the power and the angle pattern of Raman scattering and spontaneous fluorescence of active molecules in spherical microparticles steadily exposed to laser radiation. In the theoretical model used, the active fluorophore molecules were represented by a set of classical dipoles arbitrarily distributed inside the particle and excited by the electric field of the incident wave. The efficiency of excitation of every dipole was characterized by the effective polarizability of the medium at the point of its location inside the particle and was proportional to the amplitude of the principal wave. The total field of spontaneous emission was a sum of the collective field of dipole emission and some effective field caused by the particle boundary. Based on this approach, the sought parameters were calculated numerically and the analytical equations were obtained in the approximation of optically small particles.

The excitation of active molecules in a spherical resonator is characterized by the high spatial inhomogeneity of the optical pump field, manifesting itself in the volume-inhomogeneous profile of the field of spontaneous radiation. At the high power density of the radiation incident onto a particle, the probability of realization of not only one-photon transitions, but also many-photon absorption in molecules increases appreciably. Under these conditions, the function of the source inducing the spontaneous emission becomes even more inhomogeneous [26]. The one-, two-, and three-photon excited fluorescence in ethanol droplet with coumarin additions exposed to femtosecond radiation was observed experimentally in [25]. The effect of intensification of the fluorescent emission in the backward direction, opposing to the direction of the incident pump radiation, was discovered. In [25] the results were interpreted within the framework of the stationary model of the process, in which the power (integral over angles) of spontaneous fluorescence from droplets P_s

can be expressed as $P_s \propto \sigma_s^{(k)} I_L^k$, where $\sigma_s^{(k)}$ is the cross section of the k -photon absorption ($k = 1, 2, 3, \dots$); I_L is the intensity of the pump radiation in the particle. In this connection, it is important to reveal the character of this dependence at the nonstationary excitation of molecular fluorescence in the particle. For interpretation of physical and numerical experiments, it is also important to derive the analytical equations, which would allow estimation of the cross section or power of spontaneous fluorescence in microparticles exposed to short and long laser pulses.

The study of the interaction between the high-power laser radiation and aerosol is of great importance for in-depth understanding of the laser radiation propagation through the atmosphere and for remote sensing of the chemical composition of atmospheric aerosol. The transition from the nanosecond range of laser pulse duration to the femtosecond one qualitatively changes the type of nonlinear optical interactions. Thermal and ponderomotive processes are replaced by multiphoton ones. The role of nonstationary processes in light emission by microparticles increases.

In nonlinear optics of aerosols in quasi-stationary light fields, the following processes of stimulated scattering were studied: stimulated Raman scattering (SRS), stimulated Brillouin scattering (SBS), and stimulated fluorescence (SF) [27,16]. Experimental [28-30] and theoretical [29] results on the third harmonic generation (THG) in microparticles were also obtained.

New results have been obtained recently in femtosecond nonlinear optics of extended media. They are of great interest for nonlinear optics of aerosols. For femtosecond pulses with the duration t_p shorter than the period of molecular vibrations in a matter T_R , SRS manifestation has some peculiarities as compared to that under the quasi-stationary conditions. As such a pulse propagates along the Raman-active medium, every its Fourier component is converted nonlinearly. This gives rise to conversion of the entire spectrum of the pulse – it shifts to the red region [31,33].

The effect of pulse “clearing” of high-frequency components and conversion into an IR femtosecond pulse has been predicted in Ref. 34.

Another interesting fact has been discovered experimentally in Ref. 32. Stimulated molecular vibrations arose as a Raman-active medium was exposed to a group of femtosecond pulses with the repetition period equal to the period of molecular vibrations. The properties of stimulated molecular vibrations were studied from scattering of a probe light wave.

Obviously, the conditions of appearance of such effects in microparticles are different. This is connected with significantly different character of the spatiotemporal behavior of optical fields in a particle–microcavity as compared to the traveling waves.

1. The theoretical study of powerful femtosecond laser pulse filamentation in the turbulent atmosphere

Theoretical model for the nonlinear – optical pulse transformation in air

From the point of view of the nonlinear optics, the filamentation is caused by the nonstationary self-action of a femtosecond laser pulse, the peak power of which exceeds the critical power for self-focusing in air [3,9,10]. Both spatial and temporal contraction of the pulse takes place due to the Kerr nonlinearity of neutral atoms and molecules in air. As soon as the peak intensity of the radiation reaches the photoionization threshold, the free electrons are accumulated in the medium. The laser-produced plasma leads to the defocusing of the trailing part of the pulse. The front of the pulse “sees” the neutral medium and continues to self-focus at different positions along the propagation direction as predicted by the moving focus model [11]. Material dispersion in air and self-steepening of the pulse strongly contribute to the spatio-temporal dynamics of the filamentation.

Theoretical model describing the effect of diffraction, material dispersion, Kerr nonlinearity, ionization and self-steepening of the laser pulse propagating in air is based on the scalar approximation of the wave equation for the light field $q(x, y, z, t) = E(x, y, z, t) \exp\{i(\omega t - kz)\}$. From the wave equation one can obtain the nonlinear equation for the complex amplitude $E(x, y, z, t)$, which in the retarded coordinate system ($\tau = t - z/v_g$) takes the form:

$$2ik \frac{\partial E}{\partial z} = \left(1 - \frac{i}{\omega_0} \frac{\partial}{\partial \tau}\right)^{-1} \Delta_{\perp} E - k k_{\omega}'' \frac{\partial^2 E}{\partial \tau^2} + \frac{i}{3} k k_{\omega}''' \frac{\partial^3 E}{\partial \tau^3} + \\ + \frac{2k^2}{n_0} \left[\left(1 - \frac{i}{\omega_0} \frac{\partial}{\partial \tau}\right) \Delta n_k + \left(1 + \frac{i}{\omega_0} \frac{\partial}{\partial \tau}\right) \Delta n_p \right] E + \frac{2k^2}{n_0} \tilde{n}(x, y, z) E - ik\alpha E. \quad (1.1)$$

The first term on the right-hand side of the Eq.(1) describes the beam diffraction, the second and the third terms describe material dispersion, where k_{ω}'' and k_{ω}''' are the second and the third-order dispersion coefficients in air. Note that in the conditions of strong self-focusing and self-steepening, material dispersion should be considered up to the third order or higher, because the higher-order dispersion terms influence the formation of subpulses [12]. The fourth term on the right-hand side of the Eq.(1) describes the contribution of the Kerr nonlinearity and the plasma to the pulse transformation. In the fifth term random fluctuations of the refractive index in atmospheric turbulence are taken into account. The sixth term describes the pulse energy loss due to the ionization. The absorption coefficient α is given by $\alpha = I^{-1} m \hbar \omega_0 \left(\frac{\partial N_e(r, z, t)}{\partial t} \right)$, where m is the order of the multiphoton process, $I = cn_0 |E|^2 / 8\pi$ is the light field intensity.

Equation (1) for the complex amplitude of the electric field E , unlike the wave equation in the slowly varying envelope approximation (SVEA) [13], contains the operator $[1 \pm \frac{i}{\omega_0} \frac{\partial}{\partial \tau}]$. This approximation of the wave equation is called *the slowly evolving wave approximation* (SEWA) [14]. It was shown in [14] that in the

frameworks of the SEWA the equation for the complex amplitude of the electric field E accurately describes light pulse propagation down to the single cycle regime. In terms of mechanisms that contribute to the modification of ultrashort radiation, the SEWA describes self-steepening of the pulses and subpulses arising in the course of propagation as well as the shock wave formation at the back of the pulse.

The nonlinear contribution to the refractive index from the neutral molecules is considered in the form:

$$\Delta n_k(t) = (1-g) \frac{1}{2} n_2 |E|^2 + g \int_{-\infty}^t \frac{1}{2} n_2 |E(r, t')|^2 H(t-t') dt', \quad (1.2)$$

where the first term on the right-hand side of the Eq.(2) describes the instantaneous electronic response and the second term the delayed response associated with the stimulated Raman scattering on rotational transitions of molecules. In the case of oxygen and nitrogen molecules the coefficient $g=0.5$. The response function $H(t)$ was approximated based on the damped oscillator model by the following equation [10]:

$$H(t) = \theta(t) \Omega^2 \exp(-\Gamma t/2) \sin(\Lambda t) / \Lambda, \quad (1.3)$$

where $\theta(t)$ is the Heaviside function, and $\Lambda = \sqrt{\Omega^2 - \Gamma^2/4}$. The characteristic times are $\tau_1 = 2 / \Gamma = 77$ fs and $\tau_2 = 1 / \Lambda = 62.5$ fs. These values are comparable with the laser pulse duration used in the experiments on the observation of filamentation and supercontinuum generation [1-9].

The nonlinear contribution to the refractive index $\Delta n_p(x, y, z, t)$ from the laser-produced plasma is given by:

$$\Delta n_p(x, y, z, t) = - \frac{\omega_p^2(x, y, z, t)}{2n_0\omega_0^2} \quad (1.4)$$

where $\omega_p(x, y, z, t) = \sqrt{4\pi e^2 N_e(x, y, z, t) / m_e}$ is the plasma frequency, m_e and e are the electron mass and charge, respectively. The free electron density $N_e(x, y, z, t)$ depends on the spatial coordinates and time according to the kinetic equation:

$$\frac{\partial N_e}{\partial t} = R(|E|^2)(N_0 - N_e) \quad (1.5)$$

where $R(|E|^2)$ is the ionization rate, N_0 is the density of neutral oxygen or nitrogen molecules.

In the atmospheric air the large amount of free electrons comes from the oxygen molecules, the ionization potential of which $W_{O_2}=12.1$ eV is smaller than the ionization potential of the nitrogen molecules $W_{N_2}=15.6$ eV. To calculate the ionization rate $R(|E|^2)$ in the Eq.(5) we used the model [15] for the ionization of a hydrogen-like atom in the linearly polarized electric field E . This model includes the effective main quantum number $n^* = \frac{Z}{\sqrt{2E_i}}$, where Z is the effective ion charge, which allows one to introduce the fitting

parameter and to effectively take into account the difference between the ionization rates for a hydrogen-like atom and the real molecule. The value of effective charges for the ionization of O_2 and N_2 are calculated in [16]

by fitting the Eq.(5) to the experimental data on molecular ion yields. They are equal 0.53 and 0.9 for oxygen and nitrogen molecules, respectively.

Statistical characteristics of a three-dimensional field of refractive index fluctuations $\tilde{n}(x,y,z)$ are given by the model of atmospheric turbulence. For femtosecond and subpicosecond laser pulses the field $\tilde{n}(x,y,z)$ may be regarded as stationary. Statistical isotropy of the filament center wandering in the experiments [3, 17] allows us to assume that the pulse was propagated in the conditions of “the developed turbulence” obeying the Kolmogorov 11/3 law [18]. Therefore, in order to describe refractive index fluctuations in the simulations, we used the modified von Karman model of atmospheric turbulence. According to this model, the spectrum of refractive index fluctuations is given by:

$$F_n(\kappa_x, \kappa_y, \kappa_z) = 0,033 C_n^2 (\kappa + \kappa_0^2)^{-11/6} \exp(-\kappa^2 / \kappa_m^2), \quad (1.6)$$

where $\kappa_x, \kappa_y, \kappa_z$ are spatial wavenumbers. This spectrum covers both inertial and dissipative subranges of atmospheric fluctuations. Here C_n^2 is the structure constant, which characterizes the strength of turbulence; parameters $\kappa_0 = 2\pi / L_0$ and $\kappa_m = 5.92 / l_0$ are the boundaries of the spatial spectrum corresponding to the inertial subrange, L_0 and l_0 being outer and inner scales of turbulence, respectively. To generate the atmospheric phase screens with the modified von Karman spectrum of fluctuations we employ the modified method of subharmonics. [19-21]. This method increases essentially the range of spatial scales of random phase fluctuations reproduced on the grid. As demonstrated in [22], the modified method of subharmonics with four iterations of phase screen generation makes it possible to obtain random field of phase fluctuations (6), the outer scale L_0 of which is two orders of magnitude larger than the transverse size of the grid in the plane XOY .

To model the propagation through the turbulent atmosphere in the simulations, we represent the medium by a chain of phase screens located along the axis z . This chain is made up of a finite number of scattering screens and reproduces adequately the properties of continuous medium, provided the distance between the screens Δz is small compared with the characteristic scales of the field variation along the propagation coordinate z . These scales include the length of nonlinearity L_{nl} , the diffraction length L_d and the length of turbulence L_{turb} :

$$\Delta z \ll \min\{L_{nl}, L_d, L_{turb}\}. \quad (1.7)$$

The length of nonlinearity is defined as a distance along which the maximum phase growth due to self-focusing $\varphi_{nl} = n_2 k L_{nl} \max\{|E|^2\}$ does not exceed 1 radian. Then

$$L_{nl} = (n_2 k \max\{|E|^2\})^{-1}. \quad (1.8)$$

The length of turbulence L_{turb} is defined as a distance along which the mean-square deviation of the phase due to refractive index fluctuations does not exceed 1 radian. For the von Karman model of atmospheric turbulence the length of turbulence is given by:

$$L_{turb} = [2.4 \pi^2 k^2 0,033 C_n^2 (\frac{2\pi}{L_0})^{-5/3}]^{-1}, \quad (1.9)$$

The diffraction length L_d is given by the expression $L_d = ka(z)^2$. The value $a(z)$ coincides with the initial beam radius a_0 at $z=0$. Through the value $a(z)$ for $z>0$ we denote the spatial scale of the nonlinear focal region in the beam cross section.

In the course of Kerr self-focusing the intensity increases sharply in the region where a nonlinear focus is formed. Simultaneously, the lengths L_{nl} and L_d decrease. In order to satisfy the inequality (7) we decreased the interval between the phase screens as the plane of the nonlinear focus formation was approached. Since the simulation of phase screens that adequately reproduce atmospheric turbulence requires a lot of calculations we used two systems of phase screens. The first system imitates random phase fluctuations $\tilde{S}_{\text{turb}}(x,y,z)$ caused by refractive index perturbations in the atmosphere. In this system of phase screens the “turbulent” phase screens are placed equidistantly along the propagation direction with the interval Δz_{turb} . The interval Δz_{turb} is selected from both the inequality (7) and the condition governing the applicability of the δ - correlated phase screens for the turbulent atmosphere given by

$$L_0 \leq \Delta z_{\text{turb}} \ll \min \{L_{\text{turb}}, L_d\}. \quad (1.10)$$

Here L_0 is the outer scale of atmospheric turbulence defined earlier.

The second system of phase screens reproduces the nonlinear phase growth $\phi_{nl}(x,y,z)$ arising due to self-focusing. The distance Δz_{nl} between “nonlinear” phase screens decreases with increasing intensity in accordance with the conditions (7,8). In the initial stage of propagation, where the nonlinear phase growth is small and $\Delta z_{nl} > \Delta z_{\text{turb}}$, “nonlinear” phase screens are located in the same plane with the “turbulent” phase screens. Between both “nonlinear” and “turbulent” phase screens the light field undergoes only linear diffraction.

In the experiment the pulse shape and beam profile at the femtosecond laser system output are close to Gaussian, therefore, in order to solve the system of equations (1-6) we used the following initial distribution of the light field complex amplitude:

$$E(x,y,z=0,\tau) = E_0 \sqrt{\frac{\tau_0}{\tau_p(\delta)}} \exp \left(-\frac{x^2 + y^2}{2a_0^2} - \frac{\tau^2}{2\tau_p^2(\delta)} + i \frac{kr^2}{2R_f} + i \frac{\delta \tau^2}{2} \right), \quad (1.11)$$

where a_0 is the input beam radius pulse at 1/e intensity level, R_f is the geometrical focusing distance, τ_0 is a half pulse duration of a transform limited pulse at 1/e intensity level. If at the output of the compressor the pulse is chirped, then the initial pulse duration $\tau_p(\delta)$ depends on the parameter δ ($\tau_p(\delta=0)=\tau_0$), which characterizes the initial phase modulation of the pulse with a constant spectral width:

$$\delta = \pm \frac{\sqrt{(\tau_p(\delta)/\tau_0)^2 - 1}}{\tau_p^2(\delta)}, \quad (1.12)$$

The solution to the self-consistent problem (1-6) with initial conditions (11,12) defines the complex amplitude of the electric field $E(x,y,z,\tau)$ after the self-transformation of the pulse in the nonlinear random medium.

2. Researching the supercontinuum cone emission mechanism by numerical simulation of high-power femtosecond laser pulse propagation in the atmosphere

The new frequencies emerging in a femtosecond pulse while it propagates through the atmosphere might be revealed by calculating the frequency-angular spectrum $S(\theta_x, \theta_y, \Delta\omega, z)$ of the light field $E(x, y, z, t)$ at a distance z :

$$S(\theta_x, \theta_y, \Delta\omega, z) = |U(\theta_x, \theta_y, \Delta\omega, z)|^2, \\ U(\theta_x, \theta_y, \Delta\omega, z) = \int dx dy e^{-i\theta_x k_x} e^{-i\theta_y k_y} \int d\tau e^{-i\Delta\omega\tau} E(x, y, z, \tau) \quad (2.1)$$

where $\theta_x = k_x / k$, $\theta_y = k_y / k$ are the angles, at which different frequency components $\Delta\omega = \omega - \omega_0$ propagate in the medium; $\tau = t - z/v_g$ is a retarded time, v_g is a group velocity of a femtosecond pulse in air. The frequency ω_0 corresponds to 800 nm fundamental laser wavelength. For the cylindrically symmetric pulse distribution, the dependence of the angle $\theta = \theta_x = \theta_y$ on wavelength defines the supercontinuum cone emission on the blue (visible) side of the spectrum. For better understanding the conical emission phenomenon, we first describe the spatio-temporal intensity distributions arising in a single filament regime, i.e. when the peak power of the pulse is less than 10 times larger than the critical power for self-focusing in air.

To simulate the propagation we used the system of equations (1.1-1.5) with input spatio-temporal distribution of the electric field in the form of (1.11, 1.12), where $\tau_0 = 150$ fs corresponding to 250 fs FWHM, intensity $I_0 = 10^{11}$ W/cm², beam radius $a_0 = 3.5$ mm, diffraction length $L_d = ka_0^2 = 96$ m, $\delta = 0$. The pulse energy was 10 mJ and peak power $P_{\text{peak}} = 38$ GW = 6.3 P_{cr} , where P_{cr} is the critical power for self-focusing in air. Random refractive index fluctuations were not taken into account for this particular case of study.

Redistribution of the intensity in the transverse spatial direction and in time is shown in Fig.1, where the scale in the plane (r, τ) , where $r = \sqrt{x^2 + y^2}$ is chosen so that the equal intensity contours at the beginning of propagation ($z=0$) are concentric rings (Fig. 1a). At the start of the filament ($z = 0.29 L_d \approx 28$ m) the peak intensity of the pulse is attained in the temporal slice with $\tau \geq 0$ due to the delayed response of the Kerr nonlinearity (Fig.1b). The value of the peak intensity reaches $\approx 4 \cdot 10^{13}$ W/cm² and the ionization starts to defocus the trailing part of the pulse. At $z = 0.32 L_d \approx 31$ m (Fig.1c) the intensity maximum shifts towards the leading front of the pulse, its value reaches $6 \cdot 10^{13}$ W/cm². At the trailing part of the pulse rings are formed. By $z = 0.4 L_d \approx 39$ m (Fig. 1d) the diameter of the outer ring exceeds the input beam diameter by a factor of two. At the leading front we can see the very intense slices between $\tau \approx -80$ fs and $\tau \approx -50$ fs located in the narrow near-axis part within the transverse diameter of less than 300 μm . These slices form the “filament” itself, i.e. the structure that appears to a human eye as a string of light foci. Formation of dynamic multipeak structure in the spatio-temporal domain of the pulse is revealed as the spectral broadening in the frequency-angular domain.

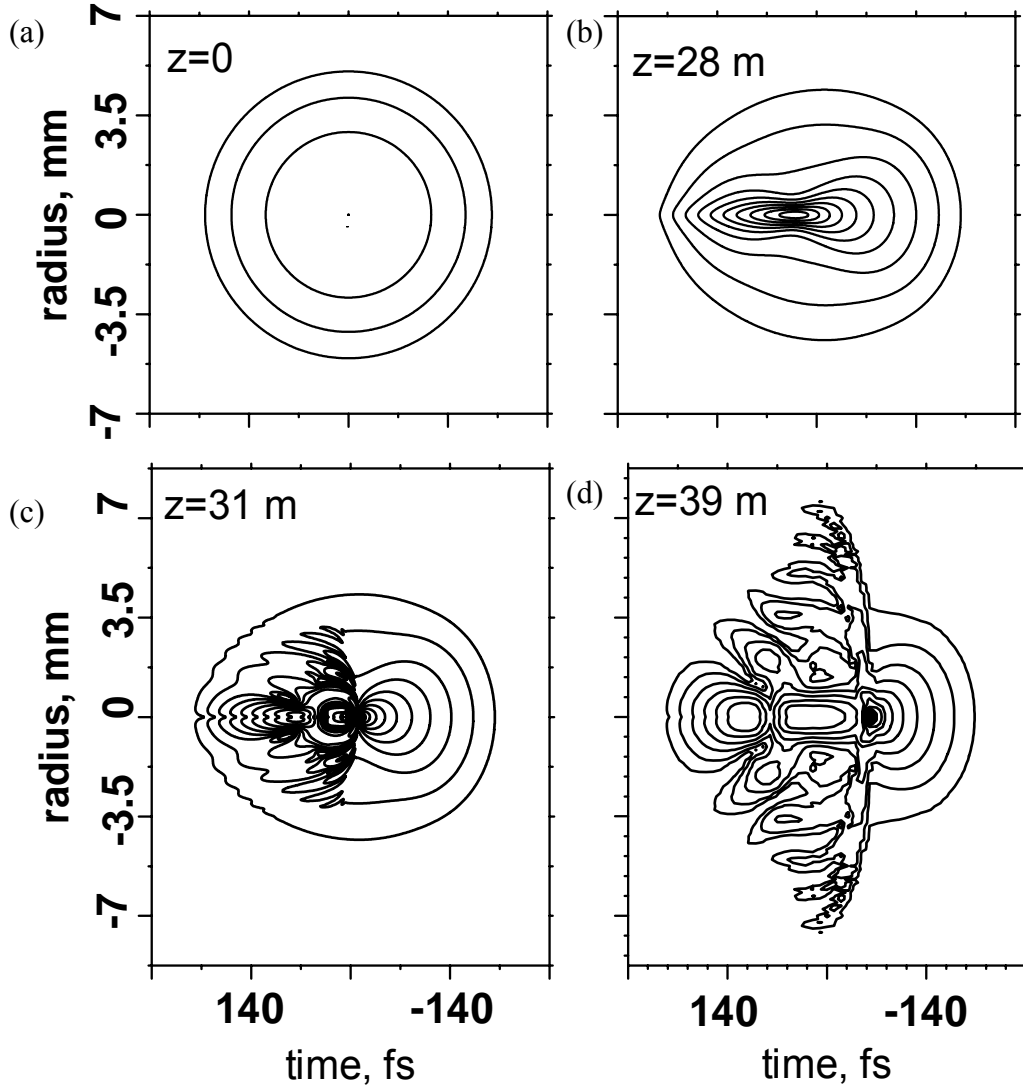


Fig. 2.1. Spatio-temporal distribution of the laser pulse intensity $I(r, \tau)$ at different distances z from the laser system output. The equal-intensity contours are plotted for the following intensity values: $I_n = I_0 \cdot 2^n$, where $n = -3, -2, \dots, +9$, $I_0 \approx 10^{11} \text{ W/cm}^2$ (a) $z = 0$; (b) $z = 0.29 L_d \approx 28 \text{ m}$; (c) $z = 0.32 L_d \approx 31 \text{ m}$; (d) $z = 0.4 L_d \approx 39 \text{ m}$.

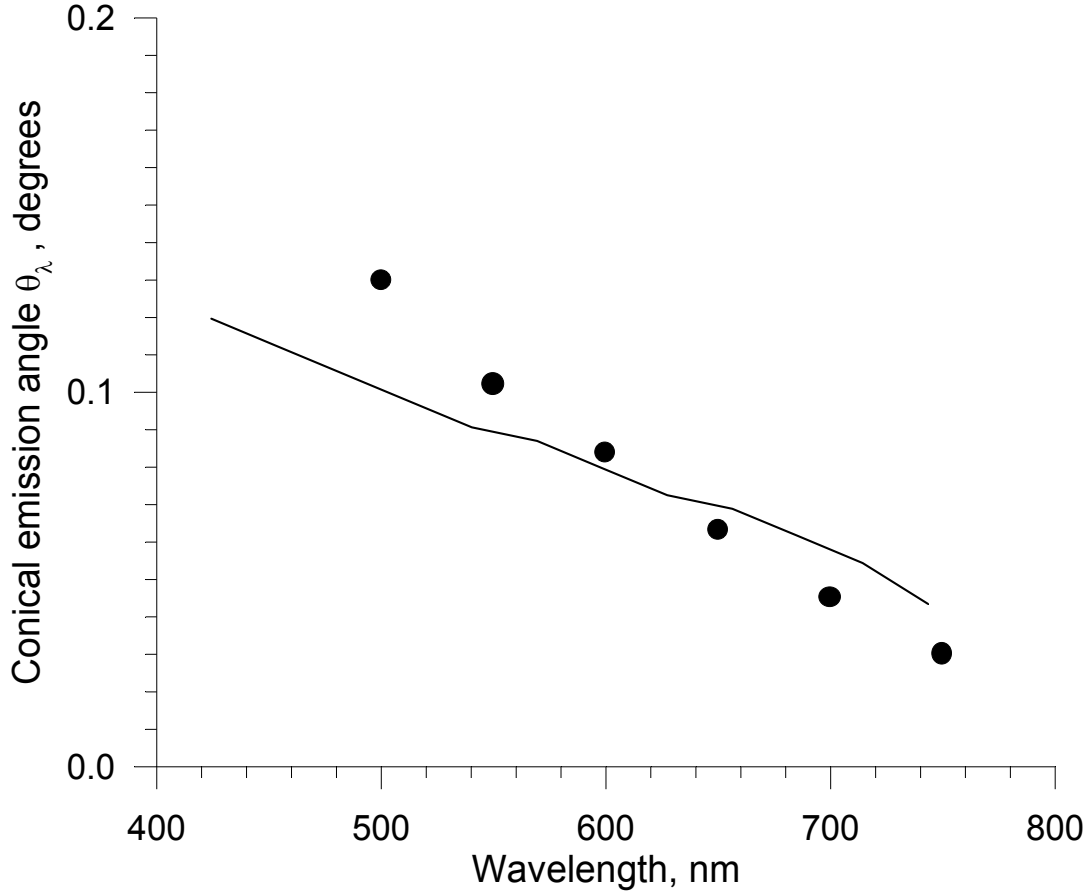


Fig. 2.2. Dependence of the conical emission angle on wavelength in the blue wing of the pulse frequency spectrum. Experimental data [9] are shown by the black dots and the simulation results by the solid curve. Both in the experiment and in the simulations pulse duration $\tau_0=150$ fs (250 fs FWHM), pulse energy is 10 mJ (the ratio of the pulse peak power to the critical power for self-focusing $P_{\text{peak}}/P_{\text{cr}}=6.3$), input beam radius $a_0=3.5$ mm, propagation distance $z=40$ m.

Because of the correct consideration of the low-intensity background of the radiation by means of simulating the actual beam diameter of $2a_0=7$ mm, without applying the spatial scaling, we were able to perform quantitative comparison between the conical emission angles obtained in the experiment (Fig. 2, symbols) and in the simulations (Fig.2, solid curve). Note, that in the previous studies [9] only the relative angles θ_λ/θ_0 , where θ_0 is the input beam divergence, could be related to the experimental data. The remaining quantitative discrepancy between the simulated and experimentally observed conical emission angles, which reaches $\approx 20\%$ for 500 nm wavelength is due to the fact that for the numerical study in this particular experimental conditions we were not able to include material dispersion into the simulations. At the same time it has been shown in [23], that the inclusion of the material dispersion leads to the increase of the conical emission angles.

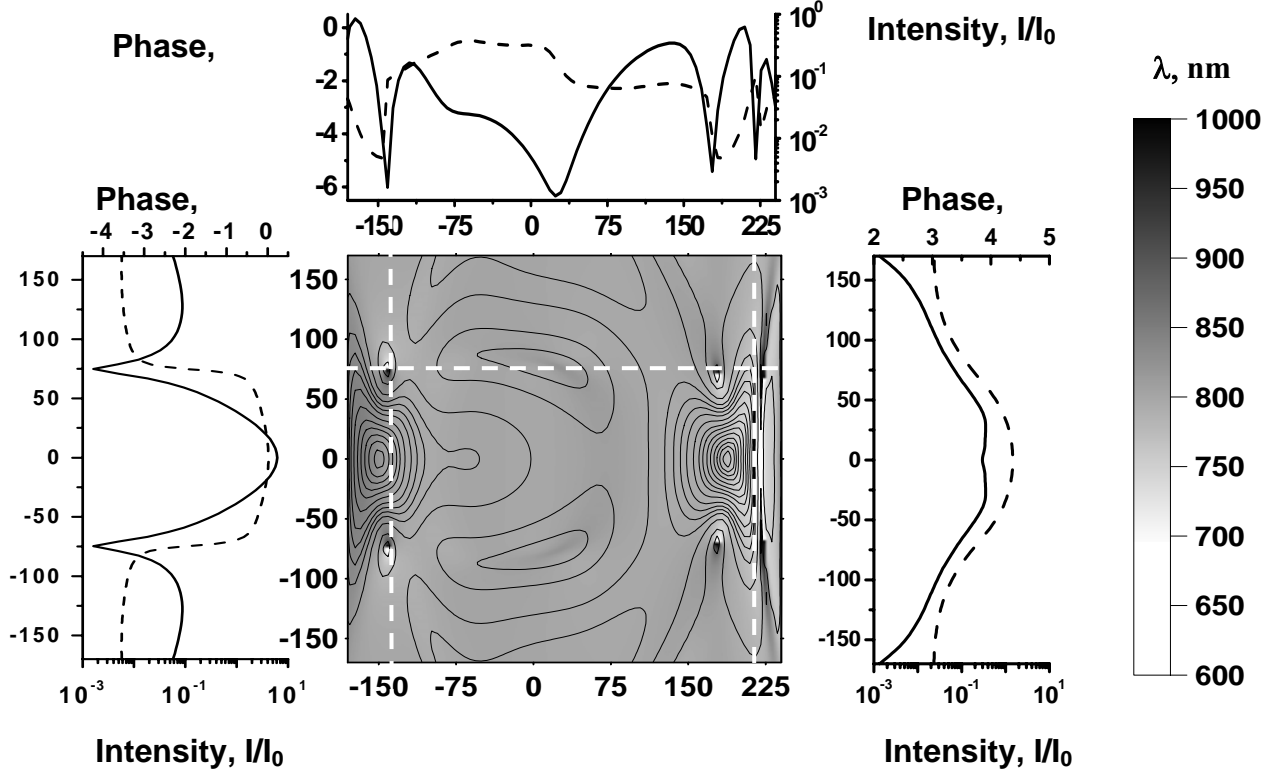


Fig. 2.3. Spatio-temporal distribution of the supercontinuum sources. The solid lines correspond to the equal-intensity contours plotted for the following intensity values: $I_n = I_0 \cdot 2^n$, where $n = -3, -2, \dots, +9$, $I_0 \approx 10^{13} \text{ W/cm}^2$. The upper inset corresponds to the temporal distribution of the pulse intensity (solid line) and phase (dashed line) at $r = 73 \text{ } \mu\text{m}$; the left and the right insets correspond to the radial distribution of the intensity (solid line) and the phase (dashed line) at $\tau = -140 \text{ fs}$ and $\tau = 217 \text{ fs}$, respectively. Propagation distance $z = 0.76L_d = 73 \text{ m}$. Pulse parameters are the same as in Fig.3. Radial position $r = 73 \text{ } \mu\text{m}$ and temporal positions $\tau = -140 \text{ fs}$ and $\tau = 217 \text{ fs}$ are indicated by the white dashed lines on the map.

For the understanding of the spectral superbroadening mechanism we study the sources of the supercontinuum in the pulse. In Fig.3 we present the map of spectral wavelengths corresponding to the frequency deviation $\delta\omega(r, \tau) = \partial\varphi(r, \tau)/\partial\tau$, where $\varphi(r, \tau)$ is the phase of the complex amplitude E . The distribution of wavelengths is presented together with the spatio-temporal intensity distribution $I(r, \tau)$ (equal-intensity contours are shown by solid lines). The upper inset in Fig.3 shows the distribution of the electric field intensity (solid line) and the phase (dashed line) as a function of time for the radial position $r = 73 \text{ } \mu\text{m}$ indicated by the white dashed horizontal line on the map. The left and the right insets in Fig.3 show the distribution of the light field intensity (solid line) and the phase (dashed line) as the function of the radial position at the leading ($\tau = -140 \text{ fs}$) and the trailing ($\tau = 217 \text{ fs}$) edges of the pulse. The temporal positions are indicated by the white dashed vertical lines on the map.

In Fig. 3 only the narrow near-axis part of the pulse distribution with the diameter of the order of 300 microns is presented. At this propagation distance $z = 0.76 L_d \approx 73$ m the intensity distribution reveals two peaks. The peak that is formed in the leading front of the pulse $\tau = -140$ fs is due to the self-focusing in air and the peak at the trailing part $\tau = 180$ fs is formed due to the joint contribution of the refocusing and the delayed Kerr response. Two distinct ring sources of the short-wavelength components in the frequency spectrum can be seen on the map. Each ring source is represented by two white points located symmetrically relatively to the beam axis $r = 0$. The first one is at the leading front of the pulse, $\tau = -140$ fs, and its radius is $73 \mu\text{m}$. This is the region, where the Kerr-induced convergence is replaced by the plasma-induced divergence of the high-intense slices. Time-dependence of the phase along the white dashed line $r = 73 \mu\text{m}$ shows the strong jump slightly before $\tau = -150$ fs and, hence, the positive frequency deviation $\delta\omega > 0$ (upper inset in Fig.3). Note, that at the same time moment $\tau = -150$ fs, the radial phase distribution, reveals a large gradient $\partial\phi/\partial r$ at the ring $r = 73 \mu\text{m}$ (left inset in Fig. 3), which means that the new high frequencies born on this ring diverge at large angles to the propagation axis. Actually, this is how the conical emission originates from the nonlinear transformation of the pulse in the conditions of self-focusing and the plasma-induced defocusing.

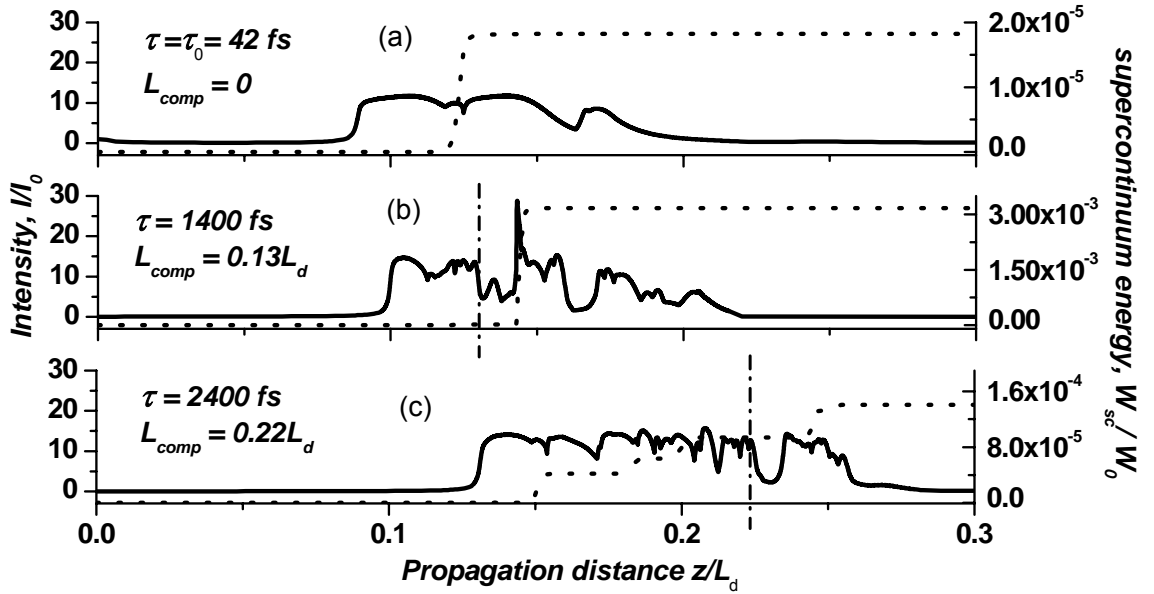


Fig. 2.4. The change of the peak intensity in the pulse with propagation distance (solid curve). The intensity $I_0 = 10^{13} \text{W/cm}^2$. The growth of the supercontinuum energy W_{sc}/W_0 (dotted curve). The laser pulse energy $W_0 = 60$ mJ, the beam radius $a_0 = 3$ cm, the geometrical focusing distance $R_f = 0.3 L_d = 2.1$ km. The compression length is indicated by the dash-dotted vertical line: (a) the compression length $L_{comp} = 0$, the pulse is transform-limited with the duration $\tau_{FWHM} = 35$ fs; (b) the compression length $L_{comp} = 0.13 L_d = 919$ m, the pulse is negatively chirped with the duration $\tau_{FWHM} = 1200$ fs; (c) the compression length $L_{comp} = 0.22 L_d = 1555$ m, the pulse is negatively chirped with the duration $\tau_{FWHM} = 2000$ fs.

The second supercontinuum source starts from the ring at the trailing edge of the pulse $\tau = 180$ fs, $r = 68 \mu\text{m}$ and persists over the whole back front $\tau > 180$ fs. Here the positive frequency deviation $\delta\omega > 0$ is due to

the shock formation at the back of the pulse, which can be also seen on the upper inset of Fig. 4, where the phase derivative $\partial\varphi/\partial\tau$ is positive at $\tau \geq 187$ fs. In the radial phase distribution at the back of the pulse ($\tau = 217$ fs, see the right inset in Fig. 3) the absolute value of the phase gradient $\partial\varphi/\partial r$ is much smaller than in the front of the pulse. In addition, there are no intensity rings, corresponding to the radial phase jumps (compare the radial intensity distributions shown by the dashed lines in the left and the right insets in Fig.3). Hence, the spatial distribution of the high-frequency components born due to self-steepening at the trailing edge of the pulse is not in the form of the conical rings.

The knowledge of such a map of the supercontinuum sources is a powerful tool for optimizing the conversion efficiency to the white light. Indeed, the increase in the conversion efficiency depends on the spatio-temporal gradients of the light field. Among the possible ways to increase the field gradients is to introduce a negative chirp into a femtosecond pulse. The negatively chirped pulse will be compressed while propagating in the medium with normal group velocity dispersion. If the compression length $L_{comp} = \tau_0^2 / k''_0$ is of the order of the self-focusing length L_{sf} , then the simultaneous spatial and temporal contraction of the radiation leads to the high spatio-temporal field gradients and large conversion efficiency to the white light. Additional parameter, which allows one to provide localization of energy in the prescribed position along the propagation direction, is the initial divergence (convergence) of the beam wavefront.

To demonstrate the possibility to govern the position of energy concentration and conversion efficiency to the white light, we have numerically studied the propagation of initially chirped and geometrically focused pulses. The parameters of the pulse in the simulations corresponded to atmospheric experiments: half duration of the transform-limited pulse and beam radius at e^{-1} intensity level were $\tau_0 = 21$ fs and $a_0 = 3$ cm, respectively, energy $W_0 = 60$ mJ, central wavelength 800 nm. The full width at half maximum (FWHM) duration corresponding to $\tau_0 = 21$ fs was $\tau_{FWHM} = 35$ fs. The beam was slightly focused at a distance $R_f = 0.3L_d$, where $L_d = ka_0^2 = 7000$ m.

Fig.4 shows the dependence of the maximum intensity and the white light energy on the propagation distance z for the pulses with different initial chirp. By the white light energy we mean the energy

$$W_{sc}(z) = \int_{\lambda_{min}}^{\lambda_{max}} S(\lambda, z) d\lambda \quad \text{contained in the short wavelength band with } \lambda_{min} = 500 \text{ nm and } \lambda_{max} = 700 \text{ nm. In the}$$

case of a transform-limited pulse with $\tau_{FWHM} = 35$ fs (Fig.4a) the supercontinuum energy W_{sc} is not higher than 0.002% of the input pulse energy. If a negative initial chirp is introduced into the pulse so that $\tau_{FWHM} = 1200$ fs (Fig.4b) and all the other parameters are the same as in the case of a transform-limited pulse, the conversion efficiency is increased by more than two orders of magnitude and reaches 0.3% of the input pulse energy W_0 . The explanation of this phenomenon is in the fact that spatial localization of energy due to geometric and nonlinear focusing is attained at the same distance as temporal localization of energy caused by the pulse compression. Indeed, the pulse with $\tau_{FWHM} = 1200$ fs is compressed down to its minimum duration at a distance $z = L_{comp} = 0.13L_d$. At the same time, the distance of the nonlinear focusing z_f can be estimated as [24]:

$$\frac{1}{z_f} = \frac{1}{z_{sf}} + \frac{1}{R_f}, \quad (2.2)$$

where z_{sf} is the self-focusing length of the collimated beam [24]. For the chirped pulse with the duration $\tau_{FWHM} = 1200$ fs the peak power is 48 GW. In air the critical power for self-focusing $P_{cr} = 6$ GW. Following [24], we estimate the self-focusing length of a collimated beam as $z_{sf} = 0.19L_d$ and the resulting length of the nonlinear focusing from the Eq.(1.1) as $z_f = 0.12 L_d$, which is close to the compression length $L_{comp} = 0.13L_d$.

The transform – limited pulse experiences temporal broadening from the start of the propagation. By the distance $z=z_{sf} = 0.02L_d$, which could be the self-focusing distance for a 35 fs 60 mJ pulse without material dispersion in the medium, the pulse duration increases up to 180 fs due to the dispersive broadening. As the result, the actual start of the filament occurs at $z = 0.09L_d$. The pulse duration at this distance is already 800 fs. The nonlinear phase gradients and the supercontinuum yield are low.

For the pulse with a longer chirp, $\tau_{FWHM} = 2000$ fs, the spatial localization occurs earlier in the propagation than the temporal localization, since $L_{comp} > z_f$ (Fig4c). Therefore, the conversion efficiency equal to $\sim 0.02\%$ to the supercontinuum is less than in the case of $\tau_{FWHM} = 1200$ fs but is still an order of magnitude larger than in the case of a transform-limited pulse.

By trying many combinations of the initial phase modulation of the pulse (pulse chirp) and geometric focusing distance we have found several optimum parameters for which the conversion efficiency to the band 500 – 700 nm increases up to 5% of the input pulse energy W_0 (see Table 2.1).

Table 2.1. Conversion efficiency to the white light in air defined as the ratio of the energy W_{sc} contained in the band 500 – 700 nm to the total input pulse energy W (expressed in percentage). The radius at e^{-1} intensity level of the input beam is a_0 . The conversion efficiency for several favorable combinations of the input pulse parameters is underlined.

Pulse duration, fs	W=60 mJ $a_0 = 15$ mm $R_f = \inf$ (parallel beam)	W=60 mJ $a_0 = 15$ mm $R_f = 0.3 ka_0^2$ (convergent beam)	W=60 mJ $a_0 = 15$ mm $R_f = -0.3 ka_0^2$ (divergent beam)
42, transform limited	0.04%	0.1%	0.002%
300, negatively chirped	<u>3%</u>	<u>5%</u>	0.6%
1200, negatively chirped	<u>2%</u>	<u>1%</u>	0.2%

Filamentation in the turbulent atmosphere

For the simulations of the filamentation in atmospheric turbulence we considered propagation of Gaussian pulses with half duration at e^{-1} intensity level $\tau_0 = 27$ fs, centered at the wavelength $\lambda = 800$ nm and peak power up to $P_0 = 0.4$ TW, which is more than 30 times greater than the critical power for self-focusing in air. Beam radius at $1/e$ level of intensity was $a_0 = 0.82$ cm. Averaging was performed over 100 pulses. Each of them was propagating through statistically independent set of phase screens simulating atmospheric fluctuations of the refractive index. The distance between two neighboring screens was $\Delta z = 10$ m. The atmospheric

structure constant C_n^2 was varied in the range $C_n^2 = 3 \cdot 10^{-15} - 15 \cdot 10^{-15} \text{ cm}^{-2/3}$, the inner scale being in the range $l_0 = 1 - 10 \text{ mm}$. Outer scale was $L_0 = 1 \text{ m}$. The atmospheric path length was 80 m.

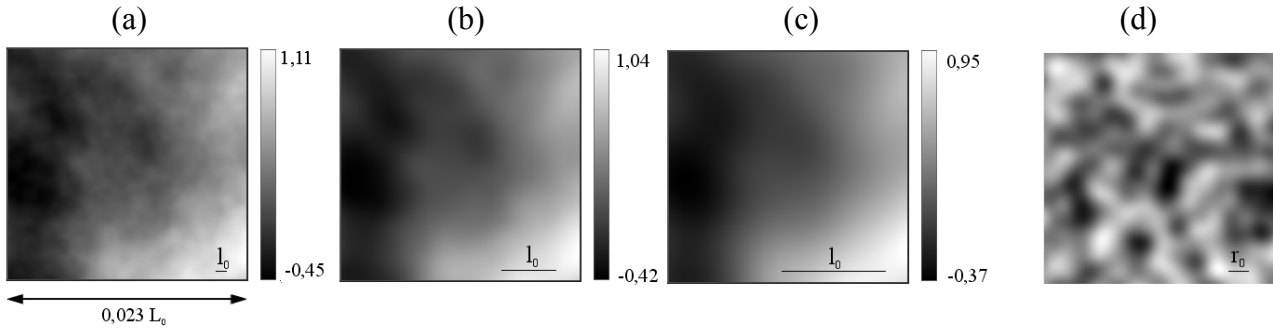


Fig. 2.5. Phase screens with the modified von-Karman spectrum (6) imitating the light field phase growth after 10 m of propagation in atmospheric turbulence with the structure constant $C_n^2 = 1.5 \cdot 10^{-14} \text{ cm}^{-2/3}$, the outer scale $L_0 = 1 \text{ m}$ and the inner scale (a) $l_0 = 1 \text{ mm}$, (b) $l_0 = 5 \text{ mm}$, (c) $l_0 = 10 \text{ mm}$. The size of the phase screen fragments is 2.3 cm x 2.3 cm (the full size is 9.2 cm x 9.2 cm). (d) The phase screen with Gaussian spectrum of random fluctuations and characteristic spatial scale 1.8 mm.

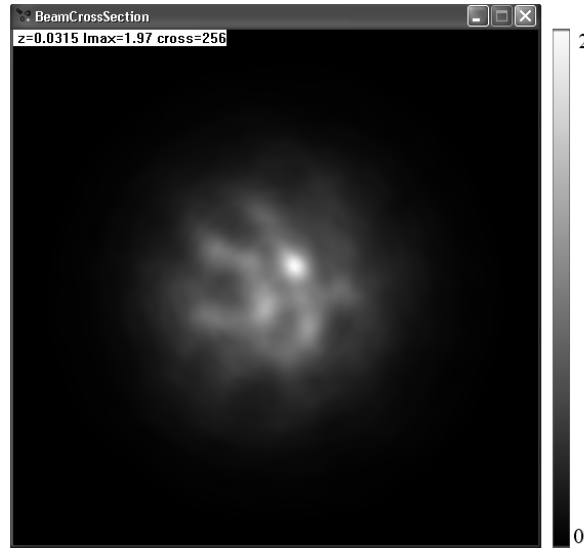


Fig. 2.6. Formation of intensity hot spot in the transverse section of a femtosecond pulse: $\tau_0 = 27 \text{ fs}$, peak power $P_0 = 2.0 \cdot 10^{11} \text{ W}$, central wavelength 800 nm, beam radius $a_0 = 0.82 \text{ cm}$, propagation distance $z = 21 \text{ m}$. Atmospheric turbulence is characterized by the structure constant $C_n^2 = 1.5 \cdot 10^{-14} \text{ cm}^{-2/3}$, the outer scale $L_0 = 1 \text{ m}$ and the inner scale (a) $l_0 = 1 \text{ mm}$.

Fig. 5 shows some chosen realizations of atmospheric phase screens generated by the modified spectral method [19-22]. Negative phase (darker colors) corresponds to focusing. The wavefront is tilted from the upper left corner towards the lower right corner. The outer scale $L_0 = 1 \text{ m}$ is the same for all the panels (a-c). The effect of the inner scale l_0 can be deduced by comparing panels a, b and c. All three panels are generated from the same set of random amplitudes; however the value l_0 changes from 1 mm (Fig.5a) to 10 mm (Fig.5c). With increasing l_0 the small-scale fluctuations are smoothed. The phase screen in Fig.5d is generated from the Gaussian spectrum. This screen contains inhomogeneities with only one spatial scale and is shown with the

purpose of comparison with phase screens generated from the von Karman spectrum (1.6). It is obvious, that a wide range of atmospheric spatial scales cannot be modeled with Gaussian phase screens.

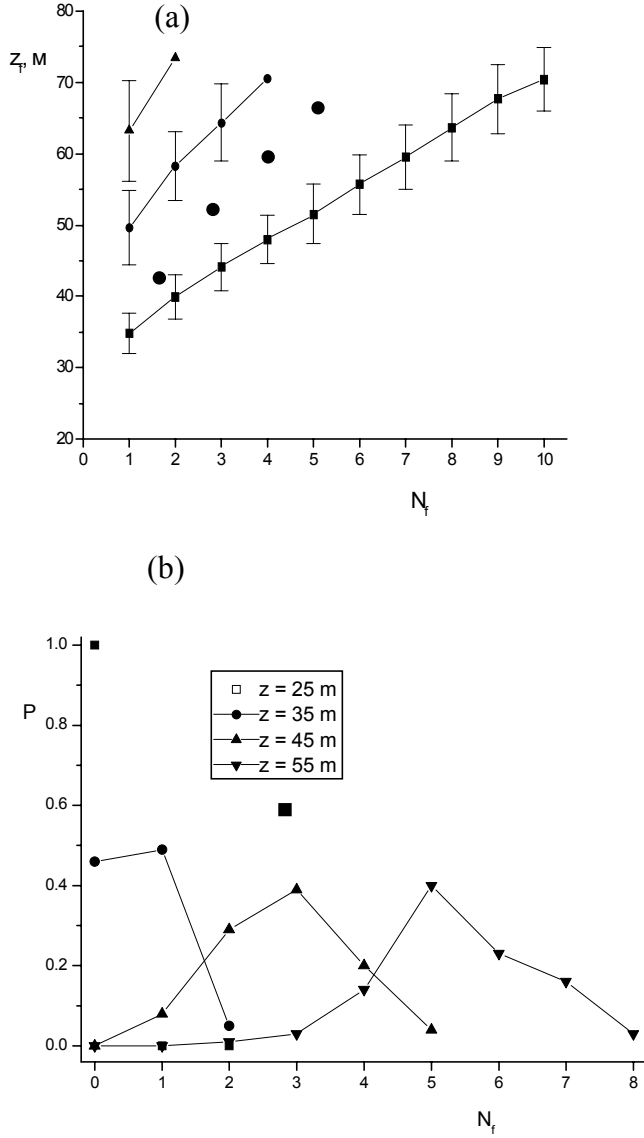


Fig. 2.7. (a) The distance z_f to the formation of the filament with the number N_f in the case of different pulse peak powers: $P_0 = 1.0 \cdot 10^{11}$ W (triangles), $P_0 = 1.3 \cdot 10^{11}$ W (circles), $P_0 = 2.0 \cdot 10^{11}$ W (squares).

(b) The probability to observe exactly N_f filaments at a given distance $z = 25$ m (squares), $z = 35$ m (circles), $z = 45$ m (upper triangles), $z = 55$ m (lower triangles). The parameters of atmospheric turbulence are $C_n^2 = 1.5 \cdot 10^{-14} \text{ cm}^{-2/3}$, $L_0 = 1$ m, $l_0 = 1$ mm.

In the central slice of the pulse and in the vicinity of intensity maximum the size of the region containing the critical power for self-focusing in air is around 1.6 mm. Therefore, we can expect that the regions with local focusing and typical size of the order of 1.6 mm will be the seeds for the filaments. The formation of a filament from the region of local focusing induced by atmospheric turbulence is illustrated in Fig.6 (white spot in the upper right part of the intensity distribution). At this distance we observe the formation of the first

filament. The subsequent filaments will be developed further in the propagation direction. Only the numerical simulations can predict their locations.

Average characteristics of multiple filaments obtained from the Monte Carlo simulations are shown in Fig.7. The distance z_f of filament formation in the turbulent atmosphere increases with the number of filaments N_f . Vertical lines indicate the root-mean-square deviation of the distance z_f from its average value. The reason for this deviation is random phase perturbations on the phase screen, which lead to different positions of filament formation in each laser shot. In the simulations a laser shot is equivalent to one realization of the chain of atmospheric phase screens along the propagation path.

The number of filaments N_f in the transverse section of the pulse increases with propagation distance (Fig.7a). The larger is the peak power of the pulse the larger number of filaments can be registered at the same distance z . Indeed, if the peak power increases twice from $P_0 = 10^{11}$ W (Fig.7a, curve marked by triangles) to $P_0 = 2 \cdot 10^{11}$ W (Fig.7a, curve marked by squares) the average distance towards the first filament formation decreases twice. At longer distances, as, for example, $z = 65$ m, the number of filaments increases from 1 in the case of $P_0 = 10^{11}$ W to 7÷9 in the case of $P_0 = 2 \cdot 10^{11}$ W. Besides, the root –mean-square deviation of the filament formation distance z_f from its average value decreases. Thus, with increasing pulse peak power, one can predict the filament formation distance with higher accuracy.

From Fig. 7 one can see that due to the random fluctuation of the filament formation distance, it is hard to predict the exact number of filaments formed from shot to shot at a given propagation distance. The probability to observe a certain number of filaments at a given distance z is shown in Fig.7b. Here, the probabilities corresponding to one propagation distance are marked by the same symbol and connected by solid lines. At a distance of $z = 25$ m (squares) the filaments will not be created for this input pulse parameters. With increase in distance to $z = 35$ m (circles) there is approximately 50% probability to observe 1 filament. Further on at $z = 45$ m (upper triangles) the probability to see multiple, namely three filaments, increases to 40%. Thus, the probability maximum shifts towards the larger number of filaments with increasing z .

Multiple filamentation in the atmosphere depends on the strength of turbulence. The stronger is the turbulence the faster is the filament formation along the propagation distance. If the structure constant C_n^2 experiences five-time increase (from $3 \cdot 10^{-15}$ to $15 \cdot 10^{-15} \text{ cm}^{-2/3}$) then the first several filaments are formed, on average, closer to the laser system output (i.e. the position $z = 0$). Instead, the increase in the inner scale of turbulence l_0 slows down the filament formation. The five-time increase in the inner scale l_0 from 1 mm to 5 mm leads to approximately one-meter delay in the formation of the first four – five filaments. The dependence of the filament formation distance on the inner scale of turbulence can be easily understood. The larger value of l_0 corresponds to the suppression of small-scale phase fluctuations. As shown earlier, exactly these small-scale fluctuations located in the vicinity of the beam top and having the typical size of the order of 1.6 mm contain the critical power for self-focusing. With the decrease in the amplitude of such fluctuations, formation of intensity hot spots in the beam slows down and delays the formation of filaments.

3. The theoretical and experimental study of the fundamental problems of scattering of a high-power femtosecond pulse in the atmosphere: nonstationary light scattering in gases and aerosols; nonlinear inelastic nonstationary light scattering by aerosols particles

3.1. Theory of nonstationary light scattering in gases and aerosols

3.1.1. Femtosecond radiation elastic scattering on a transparent spherical particle

A weakly absorbing spherical particle acts as a focusing optical system and increases the intensity of the optical radiation incident on it in the inner zones located near particle's illuminated and shadow surfaces. This increase may achieve several orders of magnitude for optically "large" particles. Up-to-date laser systems are capable of generating femtosecond pulses, whose duration is about a few optical cycles and the peak intensity is as high as $10^{12} \sim 10^{15} \text{ W/cm}^2$. Consequently, as such radiation is incident on aerosol particles due to their focusing properties it is possible to obtain even higher intensities in some local regions of the particles. This may give rise to conditions favorable for appearance of nonlinear effects, such as multiphoton and tunnel ionization, multiphoton absorption fluorescence, stimulated Raman scattering, and higher-harmonic generation. In this connection, it is important to study the dynamics of formation of the optical field intensity in spherical particles at nonstationary scattering of laser pulses to find the upper achievable level of this intensity, its spatial location, and dependence on the time parameters of the radiation, as well as the particle size.

To study the temporal evolution of the electromagnetic field inside microparticles the spectral Fourier method was applied in combination with the linear theory of diffraction, which is known as the Lorenz-Mie theory in the case of incidence of a plane monochromatic light wave on a spherical particle. In this case the initial nonstationary problem of spectral broadband radiation diffraction at a particle can be reduced to the stationary problem of scattering of a set of monochromatic Fourier harmonics. The scattering properties of the particle in this case are characterized by the, so-called, spectral response function $\mathbf{E}_s(\mathbf{r}; \omega)$, which is in fact the traditional Lorenz-Mie series written for all frequencies in the spectrum of the initial pulse [1,2].

In numerical calculations, we used the following representation for the electric field strength of the incident linearly polarized radiation:

$$\mathbf{E}^i(\mathbf{r}; t) = \frac{1}{2} \left[\mathbf{E}^i(\mathbf{r}; t) + \left(\mathbf{E}^i(\mathbf{r}; t) \right)^* \right] = \frac{1}{2} E_0 \mathbf{e}_y g(t) \cdot S(\mathbf{r}_\perp) e^{i\omega_0(t - (z + a_0)/c)} + c.c., \quad (3.1)$$

where $g(t)$ and $S(\mathbf{r}_\perp)$ are the temporal and spatial pulse profiles, respectively; ω_0 is the pulse carrier frequency; E_0 is the real field amplitude; $\mathbf{r} = \mathbf{r}_\perp + \mathbf{e}_z z$; $\mathbf{r}_\perp = \mathbf{e}_x x + \mathbf{e}_y y$; $\mathbf{e}_x, \mathbf{e}_y, \mathbf{e}_z$ are the unit vectors in the direction of the axes x, y , and z , respectively; t is time; c is the speed of light in vacuum. It was believed that the dielectric spherical particle with the radius a_0 is located at the origin of coordinates, and the laser pulse diffracting at it propagates along the positive direction of the axis z . The temporal and spatial profiles of the beam were specified by the Gaussian functions

$$g(t) = \exp \left\{ -\frac{(t - (z + a_0)/c - t_0)^2}{t_p^2} \right\}; \quad S(\mathbf{r}_\perp) = \exp \left\{ -\frac{(x^2 + y^2)}{w_0^2} \right\} \quad (3.2)$$

with the following parameters: t_p, t_0 are the pulse duration and pulse delay; w_0 is the spatial half-width.

To calculate the distribution of the internal optical field in the particle and apply the results of the stationary Mie theory, we should first pass on from the time coordinates to the spectral frequencies, representing the initial light pulse by its Fourier transform:

$$\mathbf{E}_\omega^i(\mathbf{r}, \omega) = \mathfrak{F}[\mathbf{E}^i(\mathbf{r}, t)] = E_0 \mathbf{e}_y S(\mathbf{r}_\perp) G(\omega - \omega_0) e^{-ik_0(z+a_0)}, \quad (3.3)$$

where \mathfrak{F} is the operator of Fourier transform; $G(\omega)$ is the frequency spectrum of the initial laser pulse; $k_0 = \omega_0/c$.

Equation (3) being multiplied by $e^{i\omega t}$ determines the spectral component of the initial pulse in the form of a monochromatic wave with the amplitude

$$\mathbf{A}(\omega) = E_0 \mathbf{e}_y S(\mathbf{r}_\perp) G(\omega - \omega_0). \quad (3.4)$$

Diffraction of this wave at a spherical particle is described within the framework of the stationary approximation of the Maxwell equations:

$$\text{rot } \mathbf{E}_\omega(\mathbf{r}; \omega) = -ik \mathbf{H}_\omega(\mathbf{r}; \omega); \quad \text{rot } \mathbf{H}_\omega(\mathbf{r}; \omega) = i\varepsilon_a k \mathbf{E}_\omega(\mathbf{r}; \omega) \quad (3.5)$$

where $\mathbf{H}_\omega(\mathbf{r}; \omega)$ is the magnetic field strength vector; ε_a is the complex permittivity of the particulate substance; $k = \omega/c$.

The boundary conditions on the surface of a spherical particle ($r = |\mathbf{r}| = a_0$) consist in continuity of the tangent components of the inner field \mathbf{E}_ω and \mathbf{H}_ω at transition through the surface:

$$[\mathbf{E}_\omega \times \mathbf{n}_r] = [(\mathbf{E}_\omega^i + \mathbf{E}_\omega^s) \times \mathbf{n}_r]; \quad [\mathbf{H}_\omega \times \mathbf{n}_r] = [(\mathbf{H}_\omega^i + \mathbf{H}_\omega^s) \times \mathbf{n}_r], \quad (3.6)$$

where \mathbf{n}_r is the vector of the external normal to the particle surface, and the superscript “s” corresponds to the field of the scattered wave.

Solution of Eq. (5) taking into account Eqs. (4) and (6) with the spatial profile of the light beam specified by the Gaussian function (2) leads to the following representation of, for example, the internal electric field of the particle:

$$\mathbf{E}_\omega(\mathbf{r}; \omega) = E_0 G(\omega - \omega_0) \sum_{n=1}^{\infty} \sum_{m=-n}^n R_n \left(c_{nm}(m_a k a_0) \cdot \mathbf{M}_{nm}^{(1)}(kr, \theta, \varphi) - i d_{nm}(m_a k a_0) \cdot \mathbf{N}_{nm}^{(1)}(kr, \theta, \varphi) \right), \quad (3.7)$$

where $R_n = i^n \frac{2n+1}{n(n+1)}$; $\mathbf{M}_{nm}^{(1)}, \mathbf{N}_{nm}^{(1)}$ are spherical vector-harmonics; m_a is the complex refractive index of the particulate substance. The generalized coefficients c_{nm}, d_{nm} are related to the Mie coefficients for the plane wave c_n, d_n (here we use the designations from [1]) as follows:

$$c_{nm} = c_n (g_{nm})_{TH} \quad ; \quad d_{nm} = d_n (g_{nm})_{TE},$$

where $(g_{nm})_{TH}, (g_{nm})_{TE}$ are the beam shape coefficients (BSC) being two-dimensional integrals of the radial field components of the initial beam.

Within the approach considered, the internal electric field of the particle can be written as a convolution integral of the spectrum of the initial laser pulse and the spectral response function of the particle:

$$\mathbf{E}(\mathbf{r}; t) = E_0 \mathfrak{I}^{-1} [G(\omega - \omega_0) \mathbf{E}_s(\mathbf{r}; \omega)]. \quad (3.8)$$

Here $\mathbf{E}_s(\mathbf{r}; \omega)$ denotes the series in the right-hand side of Eq. (7). Note that the scattered field can be expressed in a similar way.

The complex refractive index of the particulate substance m_a and the laser radiation wavelength λ_0 in numerical simulation were taken as $m_a = 1.33 - i \cdot 10^{-8}$ and $\lambda_0 = 0.8 \mu\text{m}$. These values correspond, for example, to water droplets illuminated by Ti:Sapphire laser pulses. The frequency dispersion of the refractive index of particles in the selected wavelength region was neglected along with the nonlinear optical effects, for example, effects of multiphoton ionization and multiphoton absorption. This neglect may lead to modification of the spatial structure of the internal optical field and, in principle, to the decrease in its intensity.

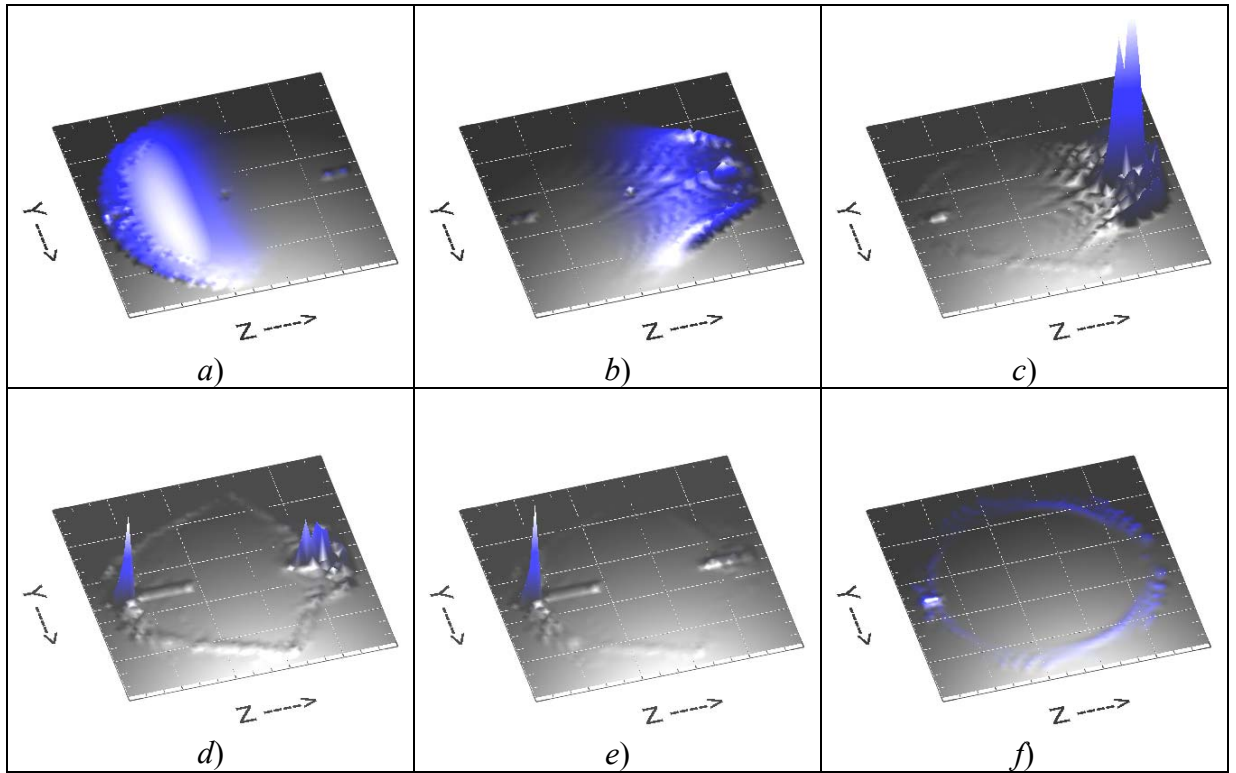


Fig. 3.1. Spatial distribution of relative intensity of the internal optical field in the main cross section of a water droplet with $a_0 = 20 \mu\text{m}$ upon its irradiation by a Gaussian beam with the parameters $\lambda = 0.8 \mu\text{m}$, $t_p = 100 \text{ fs}$, $t_0 = 200 \text{ fs}$, and $w_0/a_0 = 10$ at different time moments: $t =$ (a) 200, (b) 360, (c) 470, (d) 580, (e) 640, and (f) 800 fs. The light beam is incident from the left.

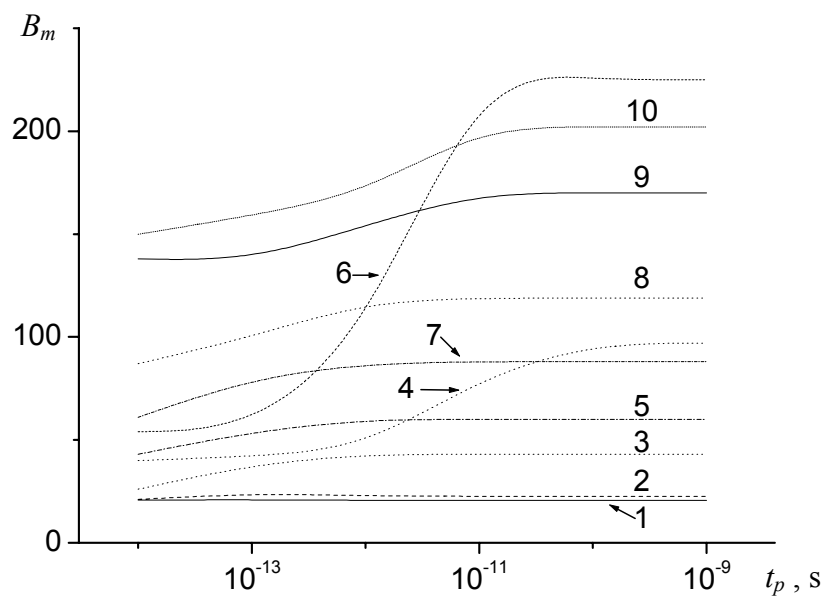
The temporal dynamics of formation of the optical field in a droplet illuminated by an ultrashort laser pulse being represented in space by a plane wave is illustrated in Fig. 1, which depict the spatial distribution of

the relative intensity of the internal field $B(\mathbf{r};t) = (\mathbf{E}(\mathbf{r};t) \cdot \mathbf{E}^*(\mathbf{r};t)) / E_0^2$ (field inhomogeneity factor) in the equatorial cross section of the particle. For clearer presentation, all the values are additionally normalized to the maximum value of the factor B in the corresponding time section.

The analysis of our simulation results shows that the spatial distribution of the internal optical field in weakly absorbing micron-sized particles illuminated by a femtosecond laser pulse has some peculiarities as compared to the case of its illumination by a monochromatic light wave.

The first peculiarity is associated with the nonstationary character of the diffraction process: there exists some transient time for establishment of the characteristic pattern of optical field focusing inside the particle. First, as the pulse propagates through the particle, the maximum of the optical field intensity spatial distribution is formed near the shadow surface; then the backward propagation of the light wave due to reflection from the inner particle surface leads to transition of the intensity maximum into the illuminated hemisphere, in which the light rays are again reflected and again form the “back” peak, thus causing the pulsating character of the time dependence of the internal field intensity. After the pulse propagates through the particle its afterglow is observed due to the delay of the radiation in the excited particle’s whispering gallery modes.

The second peculiarity is connected with the spectral width of the short laser pulse. It turns out that as such a pulse is scattering at the particle one almost always observes the resonant excitation of the internal optical field when the eigenfrequencies of one or several particle high-Q morphology-dependent resonances (MDR’s) fall in the central part of the incident pulse spectrum. This leads to the mentioned above delay of the radiation in the particle and to the decrease of the absolute maximum of the internal optical field intensity as compared to the stationary case. As the particle size increases, these effects become more pronounced. The largest decrease of the intensity maximum is observed at the exact resonance excitation, when the carrier frequency of the incident light wave matches the frequency of one of MDR’s and can achieve several orders of magnitude (see Fig. 2).



a)

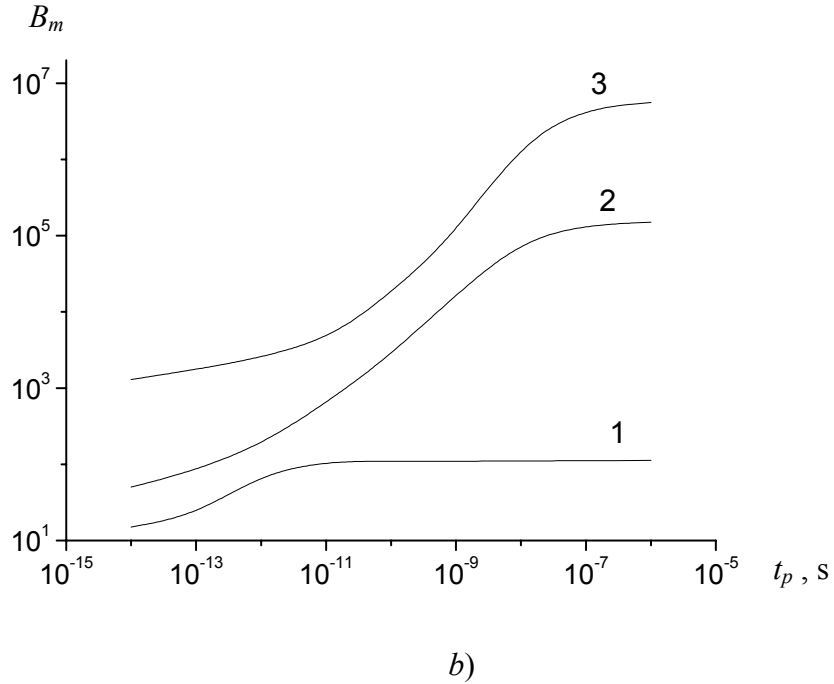
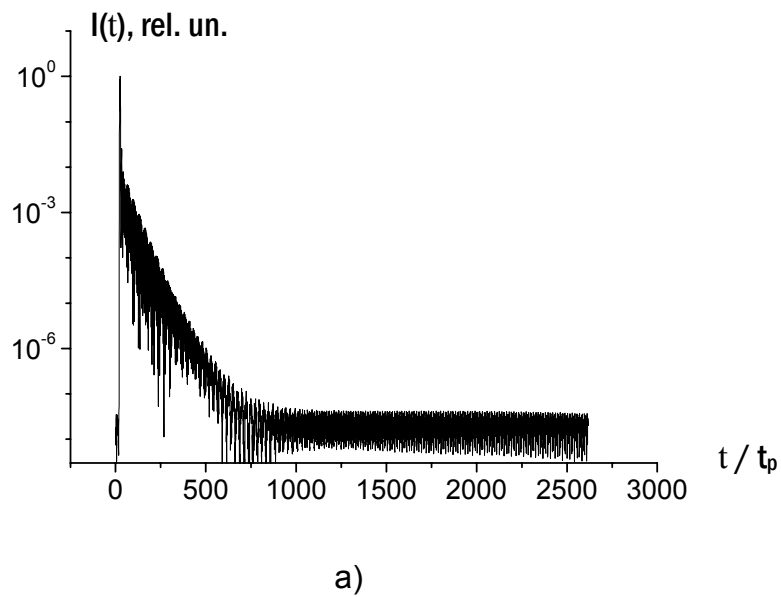


Fig. 3.2. Dependence of the maximal intensity of internal optical field B_m in a water droplet on the duration of a laser pulse t_p for various droplet sizes at not resonant (a) and resonant (b) elastic scattering. Droplet radius a_0 on fig. 1a corresponds to the following values: $a_0 = 1$ (1); 5 (2); 10 (3); 11 (4); 15 (5); 20 (6); 22 (7); 30 (8); 40 (9); 50 μm (10). For fig. 1b the radius of particles equals: $a_0 = 5.8762 \mu\text{m}$ (1); 17.133790 (2); 22.750191 (3).

Figure 3 depicts the calculated dependence of the optical fields outside a water droplet $I(t)$ (in the far zone) at diffraction of pulsed radiation with different pulse duration at it.



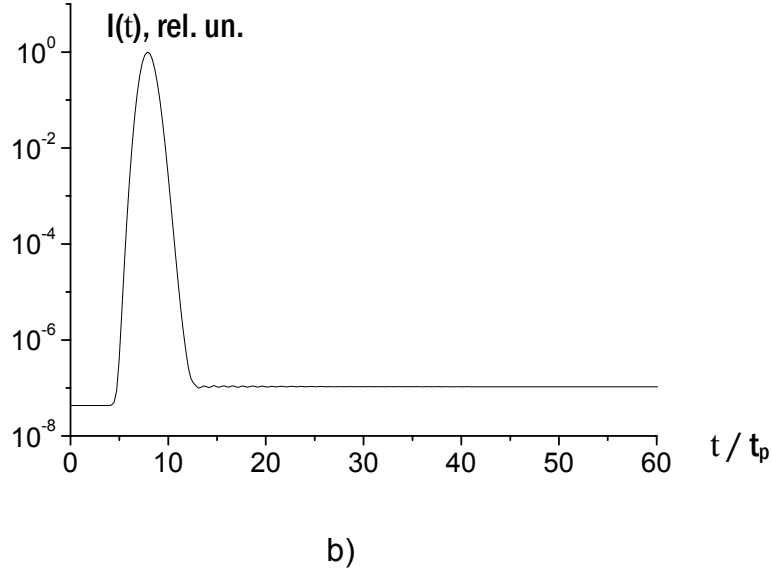


Fig. 3.3. Relative (normalized to the maximum value) intensity of the backscattered wave field as a function of dimensionless time t / t_p at scattering of pulsed radiation ($\lambda = 0.81 \mu\text{m}$, $t_p = 100$ fs (a) and 1 ps (b)) by water droplet with $a_0 = 10 \mu\text{m}$.

Elastic scattering of a train of femtosecond pulses by a transparent particle

A characteristic feature of femtosecond radiation is high time coherence in a train of pulses. This may lead to specific effects of interaction between pulses and a medium.

We studied the problem of formation of the inner field intensity in a transparent particle irradiated by a series of short pulses.

The next figures show the calculated results. It is clearly seen that in some cases the fields generated by different time-separated pulses in the particle-microcavity are added in phase. This is especially pronounced when the spectrum of the repetitively pulsed radiation coincides with strong resonance modes of the droplet.

Figures 4a–6a depict the time dependence of the relative intensity

$$B(\mathbf{r}; t) = (\tilde{\mathbf{E}}(\mathbf{r}; t) \cdot \tilde{\mathbf{E}}^*(\mathbf{r}; t)) / E_0^2$$

of the internal optical field within a water droplet in the zone of its absolute maximum B_m (shadow hemisphere) as the droplet is exposed to the train of six 100-fs pulses with the different pulse ratio. function $I_\delta(\omega)$ (dashed line) in arbitrary units (b). Figures 4b–6b show, in arbitrary units, the spectral profile of the train at these values of the pulse ratio and the function $I_\delta(\omega) = (\mathbf{E}_\delta(\omega; \mathbf{r}) \cdot \mathbf{E}_\delta^*(\omega; \mathbf{r}))$, where $\mathbf{E}_\delta(\omega; \mathbf{r})$ is the so-called spectral response of the droplet [3]. These calculations were carried out by the technique described in Refs. 1 and 4 and involving the use of the Fourier method in combination with the theory of linear light scattering.

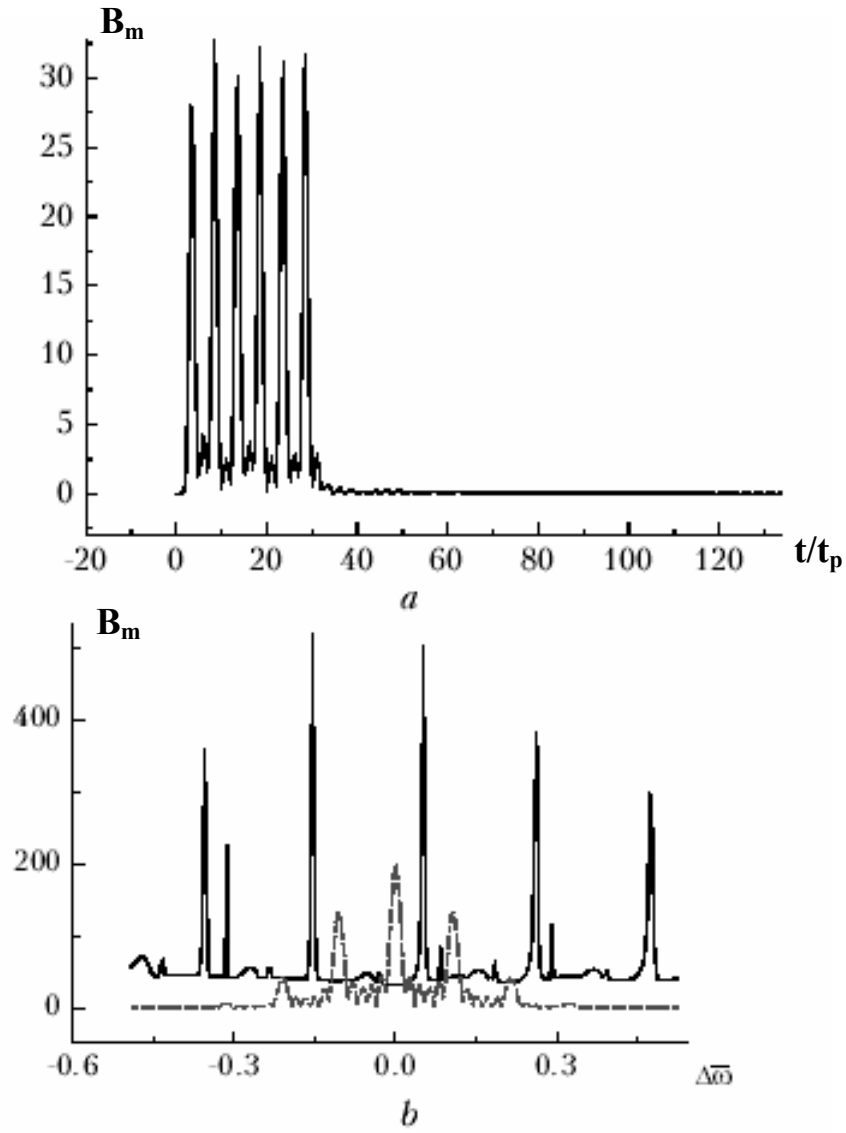


Fig. 3.4. Time dependence of the relative intensity B_m of the internal optical field within a water droplet ($a_0 = 10 \mu\text{m}$) exposed to a train of six pulses with $\lambda = 0.8 \mu\text{m}$, $t_p = 100 \text{ fs}$, and the pulse ratio $s_p = 5$ (a); the spectral profile of the train of pulses with the parameters corresponding to Fig. 4a vs. relative frequency $\Delta\bar{\omega} = (\omega - \omega_0)/\omega_0$ (solid line), and the function $I_\delta(\omega)$ (dashed line) in arbitrary units (b).

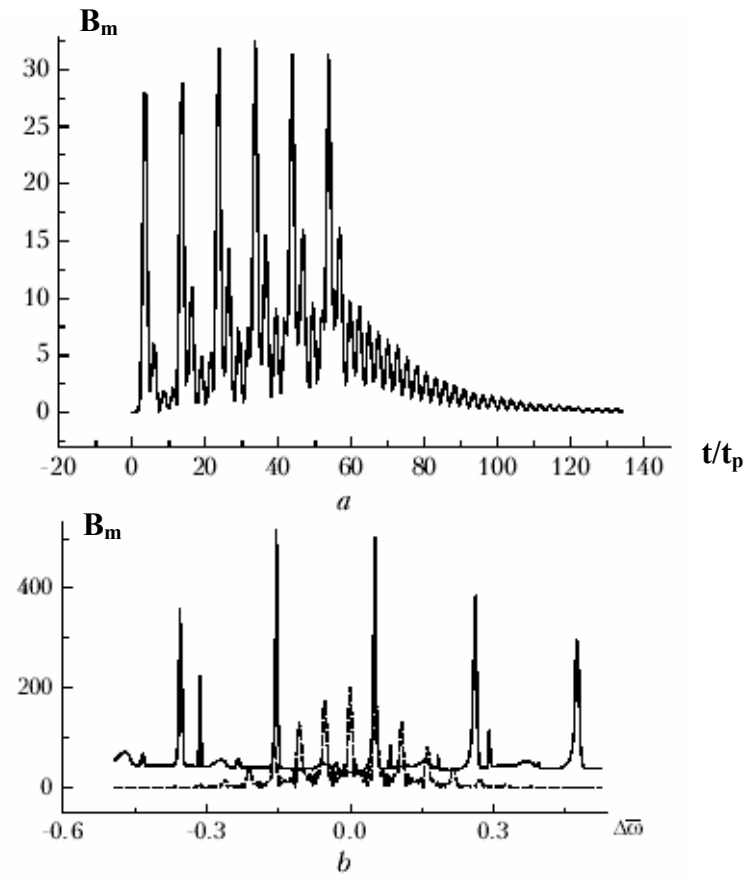


Fig. 3.5. The same as in Fig. 4a but at $s_p = 10$.

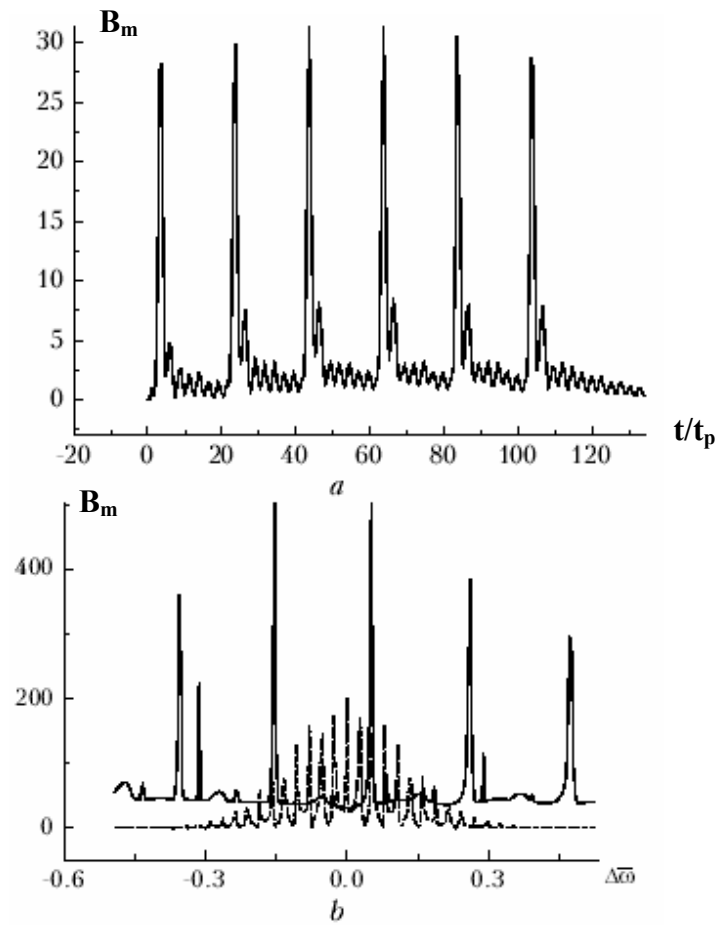


Fig. 3.6. The same as in Fig. 4a but at $s_p = 20$.

It is clearly seen from Figs. 4 –6 that in some cases the fields from individual pulses add in-phase in the particle. This is especially true, when the local spectral maxima in the train spectrum coincide with the strong resonance modes of the droplet. Thus, for example, at $s_p = 10$ and 20, when the condition $(s_p = |2\Delta\bar{\omega}_{np}|^{-1})$ is fulfilled, we can see an increase in the field intensity in the gap between pulses due to excitation of the natural mode lying just near the central frequency $TE_{85,3}$. At the same time, at $s_p = 5$ this mode is excited inefficiently.

Thus, the main difference of the repetitive scattering of pulses by a spherical microparticle from scattering by a single pulse consists in the possibility of some phasing of individual pulses in the train, when the whispering gallery modes falling within the spectral profile of the train are excited resonantly. In this case, the larger is the frequency mismatch between the natural mode and the central frequency of the incident radiation, the shorter should be the gap between the pulses.

Integral cross-section of elastic light scattering

Consider now the behavior of integral scattering characteristics, for example, the cross section of scattering by a spherical particle as a function of the pulse duration.

The time-integral cross section of scattering by a particle is calculated by the equation following from the law of energy conservation in the case of nonstationary scattering

$$\sigma_s = (W_i)^{-1} \int_{-\infty}^{\infty} dt \int_{S_r} \vec{\Pi} \vec{n}_r d\Omega, \quad (3.9)$$

where $\vec{\Pi} = \frac{c}{8\pi} \text{Re} [\vec{E}_s \times \vec{H}_s^*]$ is the Poynting vector of the scattered field, S_r is the area of a sphere with the radius $r \gg \lambda_0$ (λ_0 is the carrier wavelength in the pulse). The integral absorption cross section is, correspondingly, equal to

$$\sigma_{ab} = (W_i)^{-1} \int_{-\infty}^{\infty} dt \int_{V_a} dV \alpha_{ab} |\vec{E}|^2, \quad (3.10)$$

Thus, the integral extinction cross section can be obtained as $\sigma_{ext} = \sigma_s + \sigma_{ab}$.

Introducing the spectral factor of scattering intensity $K_s^\omega(x)$, where $x = \frac{\omega a}{c}$, and ω is the frequency inside the spectral profile of the pulse, for the integral scattering cross section we can write

$$\sigma_s = \frac{\pi a^2}{U_0} \int_{-\infty}^{\infty} d\omega G^2(\omega - \omega_0) K_s^\omega(x), \quad (3.11)$$

where $U_0 = \int_{-\infty}^{\infty} G^2(\omega) d\omega$.

Figure 7 depicts calculated $K_s = \frac{\sigma_s}{\pi a^2}$ for the radiation with $\lambda_0 = 0.81 \mu\text{m}$ versus the diffraction parameter $x_a = \frac{2\pi a}{\lambda_0}$.

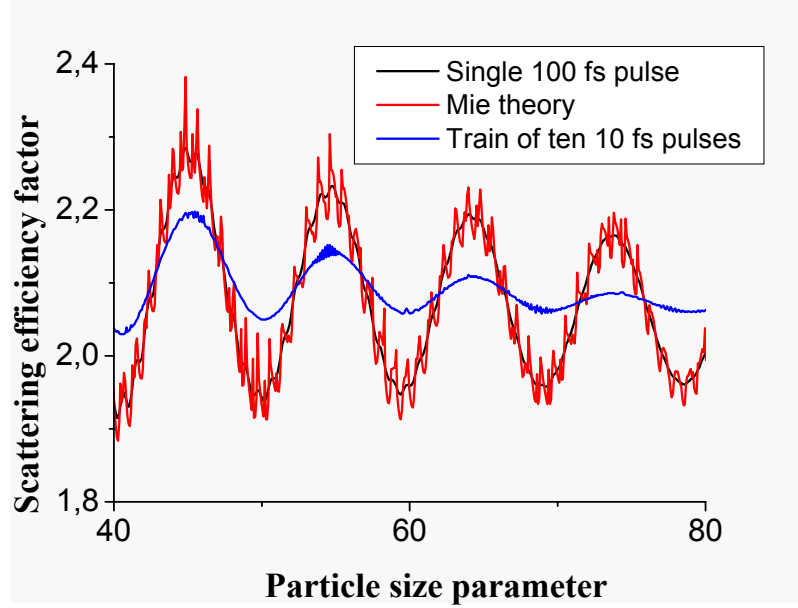


Fig. 3.7. Smoothing effect of particle optical characteristics illuminated by fs laser pulse

The results calculated agree with Shiphrin and Zolotov results, where it was noted for the first time that K_s smoothes with shortening of the pulse of femtosecond radiation. This parameter begins to tend asymptotically to 2 for femtosecond pulses with the duration < 10 fs at lower diffraction parameters than in the case of stationary radiation.

3.1.2. Linear inelastic scattering of femtosecond laser pulse on microparticle with fluorescent molecules

Consider the following formulation of the problem. A weakly absorbing, spherical particle of the radius a_0 , containing some amount of the fluorescing (active) substance, is exposed to a plane electromagnetic wave with the central frequency ω_L . It is believed that the fluorophore molecules are distributed uniformly over the particle volume and have the concentration C_0 , which is much lower than the concentration of molecules of the basic substance in the particle.

Write the wave equation for the complex vector of the electric field strength of spontaneous emission inside the particle $\mathbf{E}_s(\mathbf{r}; t)$:

$$\text{rot rot } \mathbf{E}_s(\mathbf{r}; t) + \frac{\epsilon_a}{c^2} \frac{\partial^2 \mathbf{E}_s(\mathbf{r}; t)}{\partial t^2} + \frac{4\pi\gamma_a}{c^2} \frac{\partial \mathbf{E}_s(\mathbf{r}; t)}{\partial t} = -\frac{4\pi}{c^2} \frac{\partial^2 \mathbf{P}_s(\mathbf{r}; t)}{\partial t^2}, \quad (3.12)$$

where γ_a, ϵ_a are the conductivity and permittivity of the particulate matter; c is the speed of light in vacuum;

\mathbf{P}_s is the polarization vector of the medium at the frequency of the secondary wave ω_s . The medium is believed to be nonmagnetic and isotropic; the dispersion effects are ignored. The nonlinear interaction between the waves is assumed to be weak, and pump depletion is neglected. The polarization \mathbf{P}_s in the right-hand side of Eq. (12) accounts for the field of molecular emission at the frequency of the considered dipole transition.

Represent the electric field vector of the nonlinear wave as a series in terms of the eigenfunctions of the resonator particle $\mathbf{E}_n^{TE,TH}(\mathbf{r})$, describing the spatial profile of the field of the TE and TH modes with the eigenfrequencies $\omega_n^{TE,TH}$:

$$\mathbf{E}_s(\mathbf{r};t) = \sum_n \left[A_n(t) \cdot \mathbf{E}_n^{TE}(\mathbf{r}) - iB_n(t) \cdot \mathbf{E}_n^{TH}(\mathbf{r}) \right], \quad (3.13)$$

where the coefficients A_n, B_n account for the contribution of each eigenmode to the total field [5].

We will consider only the waves with TE polarization, assuming that the analysis for the TH modes is quite analogous. The corresponding equations for the amplitudes have the form:

$$\frac{d^2}{dt^2} A_n(t) + 2\Gamma_n \frac{d}{dt} A_n(t) + \omega_n^2 A_n(t) = J_n(t), \quad (3.14)$$

where the "inducing force" is expressed in the following form:

$$J_n(t) = -\frac{4\pi}{\epsilon_a} \int_{V_a} \mathbf{E}_n^*(\mathbf{r}') \frac{\partial^2 \mathbf{P}_s(\mathbf{r}';t)}{\partial t^2} d\mathbf{r}'. \quad (3.15)$$

Here V_a is the particle volume; Γ_n is the damping coefficient of the mode due to the loss for absorption in the particulate matter and the emission of radiation through the particle surface.

A particular solution of the inhomogeneous equation (14), representing only vibrations under the effect of the "external" force, can be written as

$$A_n(t) = \frac{4\pi\hat{\omega}_n}{\epsilon_a} \int_{V_a} \mathbf{E}_n^*(\mathbf{r}') d\mathbf{r}' \left[\frac{\mathbf{P}_s(\mathbf{r}';t)}{\hat{\omega}_n} + \int_0^t \mathbf{P}_s(\mathbf{r}';t-t') e^{-\Gamma_n t'} \sin \hat{\omega}_n t' dt' \right], \quad (3.16)$$

where $\hat{\omega}_n = \omega_n \sqrt{1 - \Gamma_n^2 / \omega_n^2}$ is the natural frequency of the mode with allowance for the losses.

The macroscopic polarization $\mathbf{P}_s(\mathbf{r};t)$ of a small medium volume δV characterized by the radius-vector \mathbf{r} can be considered as a sum of dipole moments of individual molecules falling within this volume:

$$\mathbf{P}_s(\mathbf{r};t) = \sum_j^N d_j(t) \mathbf{p}_j \delta^{(3)}(\mathbf{r} - \mathbf{r}_j), \quad (3.17)$$

where N is the number of active (in terms of the considered dipole transition) molecules; \mathbf{p}_j is the vector characterizing the dipole orientation in space ($|\mathbf{p}_j| = 1$); $\delta^{(3)}(\mathbf{r} - \mathbf{r}_j)$ is the Dirac delta in the 3D space. It is well-known that the excitation of dipoles is caused by quantum fluctuations of the field (the so-called zero fluctuations of the field of vacuum), and the law of dipole emission can be represented as :

$$d_j(t) = d_0 \exp(i\omega_0 t - \Gamma_0 t), \quad (3.18)$$

where d_0 is the quantum average of the off-diagonal dipole matrix elements of the molecule; ω_0 is the frequency of the dipole transition in the molecule; $\Gamma_0 = 1/T_2$ is the damping coefficient; T_2 is the cross-relaxation time of the dipole transition.

Define the operation of averaging of an arbitrary function f over the random realizations of the characteristics \mathbf{r}_j and \mathbf{p}_j in following way:

$$\langle f \rangle = \int_{\delta V} \frac{d\mathbf{r}_j}{\delta V} \int_{4\pi} \frac{d\Omega}{4\pi} f, \quad (3.19)$$

where $d\Omega$ is an element of the solid angle. Equation (19) means that statistical averaging is performed over the position with the uniform probability density $1/\delta V$ and over orientations with the uniform probability density $1/4\pi$.

For the squared eigenmode amplitude of the nonlinear wave field of spontaneous emission, the following approximate equation can be written:

$$|A_n(t)|^2 \approx \frac{16\pi^2 |d_0|^2}{3\epsilon_a^2} \left[e^{-2\Gamma_0 t} \int_{V_a} |\mathbf{E}_n(\mathbf{r}')|^2 C(\mathbf{r}'; t) d\mathbf{r}' + \right. \\ \left. \bar{\omega}_n \int_{V_a} |\mathbf{E}_n(\mathbf{r}')|^2 d\mathbf{r}' \int_0^t C(\mathbf{r}'; t-t') e^{-\gamma_n t'} \sin \Delta\omega_n t' dt' + \frac{g_n}{4} \int_{V_a} |\mathbf{E}_n(\mathbf{r}')|^2 d\mathbf{r}' \int_0^t C(\mathbf{r}'; t-t') e^{-\gamma_n t'} F_n(t') dt' \right], \quad (3.20)$$

where $\gamma_n = \Gamma_n + \Gamma_0$ is the damping coefficient for the mode of the secondary field in the resonator; $C(\mathbf{r}; t) = N(\mathbf{r}; t)/\delta V$ is the space- and time-dependent concentration of excited molecules of the active substance; $g_n = \bar{\omega}_n^2 / (\Delta\omega_n^2 + \gamma_n^2)$ characterizes the spectral line shape of spontaneous emission in the resonator; $F_n(t) = (\Delta\omega_n \sin(\Delta\omega_n t) + \gamma_n \cos(\Delta\omega_n t))$; $\Delta\omega_n = \omega_0 - \bar{\omega}_n$.

For the two-level scheme in the approximation of weak pumping, when $N_2 \ll N_1$, where N_1 , $N_2 = N$ are the numbers of molecules at the lower and upper levels of the working transition, the corresponding equation has the form:

$$\frac{dN_2}{dt} = \frac{\sigma_{12}}{\hbar\omega_L} N_1 I_L(\mathbf{r}; t) - \Gamma_{21} N_2(t); \quad N_1 + N_2 = N_0. \quad (3.21)$$

In Eq. (21) $\sigma_{12} = \frac{4\pi\omega_0 |\mu_{12}|^2 g_L}{3c\hbar\sqrt{\epsilon_a}}$ is the absorption cross section of the one-photon transition;

$g_L = \Gamma_{21} / ((\omega_0 - \omega_L)^2 + \Gamma_{21}^2)$ is the Lorentz line width of the transition; Γ_{21} is the rate constant of the spontaneous transition; $I_L(\mathbf{r}; t)$ is the intensity of laser radiation at the principal frequency inside the particle.

The solution of Eq. (21) has the form of the convolution integral:

$$N_2(\mathbf{r}; t) = \frac{\sigma_{12}}{\hbar\omega_L} N_1 \int_0^t I_L(\mathbf{r}; t') e^{-\Gamma_{21}(t-t')} dt'. \quad (3.22)$$

For the pump wave field, we can also use the representation (13) and take into account the orthogonality of the eigenfunctions, that is, $I_L(\mathbf{r};t) = \frac{c\sqrt{\varepsilon_a}}{8\pi} \sum_m |a_m(t)|^2 \cdot |\mathbf{E}_m(\mathbf{r})|^2$ (as before, only the TE modes of the field are considered). Then, upon the substitution of $N_2(\mathbf{r};t)$ for $N(\mathbf{r};t)$ in Eq. (20), we obtain:

$$|A_n(t)|^2 = \frac{2\pi\sigma_{12}c C_0 |d_0|^2}{3\hbar\omega_L \varepsilon_a \sqrt{\varepsilon_a}} k_n^3 e^{-\Gamma_{21}t} \sum_m \Pi_{nm}^{(1)} \times \left[e^{-2\Gamma_0 t} \int_0^t |a_m(t')|^2 e^{\Gamma_{21}t'} dt' + \frac{g_n}{4} \int_0^t e^{-(\gamma_n - \Gamma_{21})t'} F_n(t') dt' \int_0^{t-t'} |a_m(t'')|^2 e^{\Gamma_{21}t''} dt'' \right], \quad (3.23)$$

where C_0 is the concentration of active molecules; $\Pi_{nm}^{(1)} = k_n^{-3} \int_{V_a} |\mathbf{E}_n(\mathbf{r}')|^2 \cdot |\mathbf{E}_m(\mathbf{r}')|^2 d\mathbf{r}'$ are the spatial overlapping integrals for the modes of the primary and secondary fields inside the particle; $k_n = \omega_n/c$.

Consider the case of short pumping of the particle, when the inequality $t_p \ll (\Gamma_{21})^{-1}$, where t_p is the laser pulse duration, is valid. Assume that the medium is excited by a rectangular pulse, and at the time $t = t_p$ the population of the upper level of the transition is maximal: $N_2^m(\mathbf{r}) \approx \frac{\sigma_{12}}{\hbar\omega_L} N_0 I_{L0}(\mathbf{r}) t_p$, and $N_2^m \ll N_0$, where $I_{L0}(\mathbf{r}) = \frac{c\sqrt{\varepsilon_a}}{8\pi} \sum_m |a_m^0|^2 \cdot |\mathbf{E}_m(\mathbf{r})|^2$ is the intensity of the principal wave inside the particle. Once the pumping is terminated ($t > t_p$), N_2 decreases exponentially with time according to Eq. (21): $N_2(\mathbf{r};t) = N_2^m(\mathbf{r}) \exp(-\Gamma_{21}(t - t_p))$. Then the squared amplitude of the mode of the secondary field takes the following form (for $t > t_p$):

$$|A_n(t)|^2 \approx \frac{\pi\sigma_{12}c |d_0|^2}{6\hbar\omega_L \varepsilon_a \sqrt{\varepsilon_a}} C_0 g_n k_n^3 t_p e^{-\Gamma_{21}(t-t_p)} \cdot \sum_m |a_m^0|^2 \Pi_{nm}^{(1)}. \quad (3.24)$$

which accounts for the relation between the damping constants:

$$\Gamma_{21} \ll \Gamma_n, \Gamma_0. \quad (3.25)$$

Introduce the variable:

$$G_s = \frac{\pi\sigma_{12}c |d_0|^2}{6\hbar\omega_L \varepsilon_a \sqrt{\varepsilon_a}}, \quad (3.26)$$

which has the meaning of the rate of transformation of the pump energy absorbed by the active molecule into the energy of its spontaneous emission. For the intensity of the field of spontaneous emission in the particle excited by a short laser pulse, we obtain the equation:

$$I_s(\mathbf{r};t) = C_0 G_s e^{-\Gamma_{21}(t-t_p)} \sum_n \sum_m g_n k_n^3 w_m^0 |\mathbf{E}_n(\mathbf{r})|^2 \Pi_{nm}^{(1)} \quad (3.27)$$

where $w_m^0 = \frac{c\sqrt{\varepsilon_a}}{8\pi} |a_m^0|^2 t_p$ is the amplitude coefficient in the corresponding expansion of the energy density of the incident wave inside the particle.

Then the total energy of spontaneous radiation emitted from inside the particle to the outside can be expressed as follows:

$$W_s = \frac{\varepsilon_a}{8\pi c^3 \Gamma_{21}} C_0 G_s \sum_n \eta_n \omega_n^4 g_n \sum_m w_m^0 \Pi_{nm}^{(1)} ; \quad t > t_p. \quad (3.28)$$

Here $\eta_n = 1 - 4\pi\gamma_a / (\varepsilon_a \hat{\omega}_n)$.

Introduce the total cross section of spontaneous emission of the particle for one-photon transitions at the nonstationary excitation $\sigma_s^{(1)}$ as a ratio of the energy of the emitted secondary field W_s to the energy density in the incident pulse. For the rectangular pump pulse, we have:

$$\sigma_s^{(1)} = \frac{W_s}{I_0 t_p} = \frac{\varepsilon_a}{8\pi c^3 \Gamma_{21}} C_0 G_s \sum_n \eta_n \omega_n^4 g_n \sum_m |\bar{a}_m^0|^2 \Pi_{nm}^{(1)}, \quad (3.29)$$

where $|\bar{a}_m^0|^2 = |a_m^0|^2 / |E_0|^2$; E_0 is the electric field strength of the incident light wave.

Consider the case of single-mode spontaneous emission. In this case, the fluorescence cross section of the particle takes the form:

$$\sigma_s^{(1)}(\omega_n = \omega_0) \cong C_0 \frac{\varepsilon_a \omega_0^4}{8\pi c^3 \Gamma_{21}} G_s \eta_n \frac{\omega_0^2}{(\Gamma_n + \Gamma_0)^2} [\Pi^{(1)}]_{eff} V_a \bar{B}_L(x_a). \quad (3.30)$$

If the dominant mode is a high-Q mode, that is $\Gamma_n \ll \Gamma_0$, then the fluorescence cross section is inversely proportional to the squared natural line width of spontaneous emission Γ_0 . Otherwise, for the low-Q mode ($\Gamma_n \gg \Gamma_0$), the main contributor to $\sigma_s^{(1)}$ is the natural damping of the resonator.

Compare Eq. (30) with the spontaneous fluorescence cross section of an extended medium $\sigma_{s\infty}^{(1)}$. The ratio of the fluorescence cross section of the particle in the case of excitation of a single mode of the secondary field to that in a spherical region without pronounced resonator properties, containing the same number of active molecules and having the same volume as the particle, is the following:

$$\sigma_s^{(1)} / \sigma_{s\infty}^{(1)} = \frac{1}{(1 + \Gamma_n / \Gamma_0)^2} \bar{B}_L [\Pi^{(1)}]_{eff}. \quad (3.31)$$

For numerical estimates, let us consider a water drop with the refractive index $n_a = 1.33$. At the mean value of the overlapping integral $[\Pi^{(1)}]_{eff} \approx 20$, we have the sought ratio of the fluorescence cross sections in the absence of input resonance ($\bar{B}_L \sim 2$): $\sigma_s^{(1)} / \sigma_{s\infty}^{(1)} \sim 0.1$ for low-Q modes ($\Gamma_n \gg \Gamma_0$) and $\sigma_s^{(1)} / \sigma_{s\infty}^{(1)} \sim 40$ for high-Q modes ($\Gamma_n \ll \Gamma_0$). At the resonance excitation of spontaneous fluorescence by the incident wave (conditions of input resonance), when $\bar{B}_L \gg 1$, these estimates should be increased by more than order of magnitude.

Thus, at excitation of spontaneous fluorescence in microparticles, the spectral cross section of the one-photon process for some modes can exceed the spontaneous emission cross section of the same volume of an extended medium, and this excess is proportional to the product of the factors accounting for the focusing properties of the particle and its characteristics as a dielectric microresonator. The spherical shape stipulates appearance of local maxima in the spatial intensity distribution of the pump field and the field of the secondary wave inside the microparticle and, consequently, the more efficient excitation of active molecules in the zones of local maxima as compared to the extended medium. It can be stated that just this is the main reason for asymmetry in the angular distribution of the fluorescence field from particles, which was repeatedly observed in the experiments (see, for instance, [6]), while the spontaneous fluorescence of a bulky substance is characterized by the isotropic angular distribution.

3.1.3. About linear nonstationary light scattering in gases

Our researches have shown that the linear scattering of ultra-short radiation on gaseous media has no appreciable differences from its stationary analogue, therefore for estimations of integral scattering characteristics under the condition of non-stationary process it is possible to use results of the stationary theory.

3.2. Nonlinear inelastic nonstationary light scattering by aerosols particles

3.2.1. Nonlinear-optics effects of high-power femtosecond radiation in microparticles

A characteristic feature of the interaction of high-power femtosecond radiation with aerosol particles is the absence of thermal nonlinear effects because of the short pulse duration. The main effects in this case are multiphoton absorption, multiphoton ionization and other effects associated with optical anharmonism.

In what follows, we concentrate our attention at representation of the results of nonlinear femtosecond optics for liquid-droplet aerosols. We start from the model of macroscopic nonlinear optics, in which the vector of macroscopic nonlinear polarization of the medium is introduced as

$$\mathbf{P}_N = \sum^N \langle \boldsymbol{\mu}_N \rangle, \quad \langle \boldsymbol{\mu}_N \rangle = S_p(\rho \boldsymbol{\mu}), \quad (3.32)$$

where $\langle \boldsymbol{\mu}_N \rangle$ is the mean dipole moment of the molecule as found from solution of the classical or quantum problem under the conditions of nonlinear interaction.

In liquid transparent media, nonlinear effects are connected, in the first turn, with the so-called cubic nonlinearity of the medium

$$\mathbf{P}_N = \hat{\chi}^{(3)} \mathbf{E} \mathbf{E} \mathbf{E}. \quad (3.33)$$

The imaginary part of the tensor of cubic susceptibility describes generation of the Stokes radiation, third harmonic generation, and two-photon luminescence.

3.2.2. Nonlinear interactions of optical fields of femtosecond pulse in a microparticle connected with anharmonism

Let us first write the most general equation characterizing nonlinear optical interactions in the particulate matter. The effects of nonlinear optics of ultrashort pulses are connected with the presence of the third-order nonlinear polarization of the medium [7]. The corresponding real vector of nonlinear polarization \mathbf{P}_{nl} can be presented in the following form [8]:

$$\mathbf{P}_N = N_0 Q_m \mathbf{E} + \hat{\chi}_e^{(3)} \mathbf{E} \mathbf{E} \mathbf{E}. \quad (3.34)$$

In Eq. (34) the first term is responsible for the contribution from Raman scattering to nonlinear polarization of the medium, and the second term describes the contribution due to the electronic polarizability leading to the third harmonic generation. The designations are the following: \mathbf{E} is the real vector of the electric field in the medium; N_0 is the number of molecules in a unit volume; Q_m is the coordinate of nuclei displacement in a molecule; $\hat{\chi}_e^{(3)}$ is the tensor of third-order electronic susceptibility of the matter. For a fluid, the role of the second-order susceptibility leading, in particular, to the second harmonic generation is very small. Note that the electronic susceptibility follows the field almost immediately. At the same time, the SRS effect occurs in a certain delay.

Nonlinear polarization is the source of nonlinear optical waves in the particle. The equation for the electric field has the form

$$\text{rotrot} \mathbf{E}(\mathbf{r}, t) + \frac{\varepsilon_a}{c^2} \frac{\partial^2 \mathbf{E}(\mathbf{r}, t)}{\partial t^2} + \frac{4\pi\sigma}{c^2} \frac{\partial \mathbf{E}(\mathbf{r}, t)}{\partial t} = -\frac{4\pi}{c^2} \frac{\partial^2}{\partial t^2} \mathbf{P}_N(\mathbf{r}, t), \quad (3.35)$$

where ε_a and σ are the dielectric constant and conductivity of the particulate matter, respectively. Then for the pumping wave (subscript “L”) and Stokes wave (subscript “S”) we can write down two equations:

$$\begin{aligned} \text{rotrot} \mathbf{E}_S(\mathbf{r}; t) + \frac{\varepsilon_a}{c^2} \frac{\partial^2 \mathbf{E}_S(\mathbf{r}; t)}{\partial t^2} + \frac{4\pi\sigma}{c^2} \frac{\partial \mathbf{E}_S(\mathbf{r}; t)}{\partial t} &= -\frac{4\pi}{c^2} \frac{\partial^2 \mathbf{P}_N^S(\mathbf{r}; t)}{\partial t^2} \\ \text{rotrot} \mathbf{E}_L(\mathbf{r}; t) + \frac{\varepsilon_a}{c^2} \frac{\partial^2 \mathbf{E}_L(\mathbf{r}; t)}{\partial t^2} + \frac{4\pi\sigma}{c^2} \frac{\partial \mathbf{E}_L(\mathbf{r}; t)}{\partial t} &= -\frac{4\pi}{c^2} \frac{\partial^2 \mathbf{P}_N^L(\mathbf{r}; t)}{\partial t^2}, \end{aligned}$$

where electric fields inside a particle are represented by a series in terms of cavity eigenfunctions \mathbf{E}_{np}^{TE} and \mathbf{E}_{np}^{TH} :

$$\mathbf{E}_{L,S}(\mathbf{r}; t) = \sum_{n=1}^{\infty} \sum_{p=1}^{\infty} \left[A_{np}^{L,S}(t) \mathbf{E}_{np}^{TE}(\mathbf{r}) - i B_{np}^{L,S}(t) \mathbf{E}_{np}^{TH}(\mathbf{r}) \right]$$

We have obtained the equations for the time coefficients of the fields of different types of nonlinearity:

$$\frac{d^2}{dt^2} A_{np}^{L,S}(t) + 2\Gamma_{np}^{L,S} \frac{d}{dt} A_{np}^{L,S}(t) + \omega_{np}^2 A_{np}^{L,S}(t) = J_{np}^{L,S}(t),$$

where

$$J_{np}^L(t) = F_{np}^i(t) + \frac{4\pi}{\varepsilon_a} \int_V \mathbf{E}_{np}^* \frac{\partial^2 \mathbf{P}_N^L}{\partial t^2} d\mathbf{r}$$

$$J_{np}^S(t) = -\frac{4\pi}{\varepsilon_a} \int_V \mathbf{E}_{np}^* \frac{\partial^2 \mathbf{P}_N^S}{\partial t^2} d\mathbf{r}$$

Analysis of the equations revealed the thresholds of the processes and the characteristic dependences of the energy parameters (intensity, energy) on the power parameters of the femtosecond pulse and medium characteristics.

The medium is assumed homogeneous inside the particle. The coordinate Q_m is determined by the equation of forced vibrations:

$$\frac{\partial^2 Q_m}{\partial t^2} + \frac{2}{T_2} \frac{\partial Q_m}{\partial t} + \Omega_R^2 Q_m = F(t), \quad (3.36)$$

where $F(t) = \frac{1}{2m} \frac{\partial \alpha}{\partial Q_m} n_m |\mathbf{E}|^2$ is the force; α is the medium polarizability; m is the molecular mass; T_2 is the time of cross relaxation; Ω_R is the frequency of molecular vibrations; $n_m = (N_1 - N_2)/N_0$, $N_{1,2}$ are populations of the levels involved in the Raman active transition $1 \rightarrow 2$. The equation for n_m has the following form:

$$\frac{\partial n_m}{\partial t} + \frac{n_m - 1}{T_1} = \frac{1}{2\hbar\Omega_R} \frac{\partial \alpha}{\partial Q_m} |\mathbf{E}|^2 \frac{\partial Q_m}{\partial t}, \quad (3.37)$$

where T_1 is the time of longitudinal relaxation; \hbar is the Planck's constant.

The solution for the coordinate Q_m is well known:

$$Q_m = \frac{1}{2m} \frac{\partial \alpha}{\partial Q_m} \exp(-t/T_2) \int_0^t F(t') \exp(-t'/T_2) \sin \Omega_R(t-t') dt'. \quad (3.38)$$

A peculiarity of the behavior of the coordinate Q_m in the microparticle is that, due to the excitation of WG modes in it, the characteristic properties of ultrashort pulses ($t_p \ll T_2$ or $t_p < \Omega_R^{-1}$) in no way do manifest themselves. This is connected with the fact that time behavior of the function F for the WG modes is determined by the modes' lifetimes rather than by the duration of a femtosecond laser pulse, as for the case of propagation of a traveling wave.

Our consideration is based on the physical model, in which whispering-gallery modes are formed as the pulse passes through the particle (for the time $\tau_r \sim 2\pi a_0/c$), whereas no significant processes of nonlinear scattering occur in the particulate matter. If the modes formed by the femtosecond pulse include such that their frequencies ω meet the condition of Raman resonance $\omega_S \approx \omega_L - \Omega_R$, then the process of amplification of one mode with the frequency ω_S by the other mode with the frequency ω_L becomes possible.

For the time moment $t > t_p$ the intensity in the WG mode, in the absence of a nonlinearity, can be presented as

$$I_{WG}(\omega_{L,S}, t) = I_{WG}(\omega_{L,S}, t_p) \exp\left\{-\left(t - t_p\right) \omega_{L,S} / Q_{L,S}\right\}. \quad (3.39)$$

Here $Q_{L,S}$ are the Q-factors for the corresponding modes. Since the lifetime of the modes is $\tau_r \sim 10^{-9} - 10^{-7}$ s, the process of nonlinear interaction among the modes for such times can be considered in the quasistationary approximation. In this case, nonlinear polarization connected with the SRS process is formed in the medium. The vector of nonlinear polarization can be written as

$$\mathbf{P}_R^{(3)}(\omega_S) = \chi_R^{(3)}(\omega_S) (\tilde{\mathbf{E}}_L \tilde{\mathbf{E}}_L^*) \tilde{\mathbf{E}}_S + c.c. \quad (3.40)$$

In Eq. (40), $\tilde{\mathbf{E}}_{L,S}$ are complex electric fields of the modes L and S ; $\chi_R^{(3)}(\omega_S)$ is nonlinear susceptibility of the medium for the SRS effect. Under conditions of SRS resonance

$$\chi_R^{(3)} = -i \frac{N_0 T_2}{16 m \Omega_R} \left(\frac{\partial \alpha}{\partial Q_m} \right)^2. \quad (3.41)$$

The equations describing mode interaction at SRS in a microparticle were derived in Ref. 9 in the quasistationary approximation. We use here these results, as well as the approximation of the given field of the pump mode. For the intensity of the Stokes mode we have

$$\begin{aligned} I_{WG}(\omega_S, t_p) &= I_{WG}(\omega_S, t_p) \exp \left\{ \int_{t_p}^t g I_{WG}(\omega_L, t') dt' - \frac{(t - t_p) \omega_S}{Q_S} \right\} \approx \\ &\approx I_{WG}(\omega_S, t_p) \exp \left\{ \frac{g I_{WG}(\omega_S, t_p) Q_L}{\omega_L} \times \left[1 - \exp \left\{ -\left(t - t_p\right) \omega_L / Q_L \right\} \right] - \frac{(t - t_p) \omega_S}{Q_S} \right\}, \end{aligned} \quad (3.42)$$

where $g = \frac{c g_s B_c}{n_a}$, $g_s = \frac{2 \pi N_0 \omega_S T_2}{c^2 \epsilon_a m \Omega_R} \left(\frac{\partial \alpha}{\partial Q_m} \right)^2$ is the coefficient of the Stokes wave intensification; B_c is the coefficient of spatial overlapping of the fields of the modes L and S [10].

Equation (42) shows that SRS leads to a decrease in the damping factor of the Stokes mode. The maximum intensification increment that is possible in the mode of the Stokes frequency can be expressed as follows:

$$G_{\max} = \frac{c g_s B_c I_{WG}(\omega_L, t_p) Q_S}{n_a \omega_S}. \quad (3.43)$$

Let us assume that $I_{WG} \approx I_0 \frac{\Delta \omega_L}{\Delta \omega_p}$, where I_0 is the maximum intensity in the femtosecond pulse. The width of the WG modes is $\Delta \omega_L = \omega_L / Q_L$. Thus, we obtain

$$G_{\max} = \frac{c g_s B_c I_0 Q_S \omega_L \tau_p}{n_a \omega_S Q_L 4 \pi}. \quad (3.44)$$

The effective coefficient of SRS amplification in the microcavity is introduced as: $g_e = g_s B_c$, where g_s is steady-state Raman gain; ω_s is Stokes frequency; Q_s is MDR's quality factor;

$$\bar{B}_L = \frac{\bar{I}_L}{I_0} = \frac{1}{V_a E_0^2} \int_{V_a} \mathbf{E}_L(\mathbf{r}) \mathbf{E}_L^*(\mathbf{r}) d\mathbf{r}, \quad (3.45)$$

and B_c is the normalized coefficient of spatial overlap of interacting fields inside the particle. The coefficient B_c weakly depends on time both at the initial stage and at the stage of steady state SRS. At the initial stage of the process, it can be calculated separately in the linear approximation, that is, within the Mie theory:

$$B_c = V_a \left[\int_{V_a} (\mathbf{E}_L \cdot \mathbf{E}_L^*) d\mathbf{r} \times \int_{V_a} (\mathbf{E}_S \cdot \mathbf{E}_S^*) d\mathbf{r} \right]^{-1} \times \int_{V_a} (\mathbf{E}_L \cdot \mathbf{E}_L^*) (\mathbf{E}_S \cdot \mathbf{E}_S^*) d\mathbf{r}. \quad (3.46)$$

The coefficient g_e reflects the difference in the rate of the Stokes wave generation in the particle as compared with the extended medium. This leads to a significant decrease of the process thresholds and in some cases allows the continuous-wave radiation to be used to pump the microcavity.

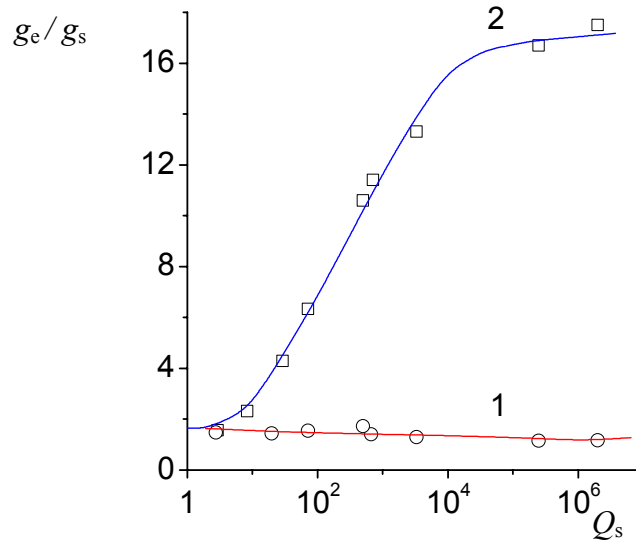


Fig. 3.8. The dependence of g_e/g_s ratio on the Q-factor for the resonance modes Q_s of the Stokes field at excitation of the SRS due to single (1) and double (2) fields resonance. Solid line is a guide for eye.

Figure 8 shows the dependence of the g_e/g_s ratio on the effective Q-factor of the Stokes field eigenmodes Q_s . The calculation was performed for water droplets of different radius ($n_a = 1.33$, $\lambda_L = 0.53 \mu\text{m}$, $\lambda_s = 0.65 \mu\text{m}$) in two situations of nonlinear interaction between waves: resonance of only the Stokes field (“single” resonance) and resonance of both waves (“double” resonance). It follows from this figure that the ratio g_e/g_s is close to unity at nonresonance SRS excitation. A significant growth of the efficiency of nonlinear interaction is observed only in the case of double resonance between the fields.

Let us emphasize once more that the considered excitation threshold of the Raman wave corresponds, in fact, to fulfillment of the condition for appearance of positive feedback in the particle-cavity for the Stokes wave, when its total loss due to absorption and emission through the particle surface becomes equal to the gain due to nonlinear interaction with the pump field. The intensity of stimulated scattering under such conditions is low and corresponds to the intensity of spontaneous Raman scattering.

The value of G_{\max} depends significantly on the degree of spatial overlapping of the modes – the coefficient B_c . To estimate it reliably, additional investigations are needed. Assuming that $B_c = 1$, for $\omega_L = 3542$ THz, $\omega_S = 2898$ THz, $g_s = 10^{-3}$ cm/MW, $Q_S = Q_L$, and $\tau_p = 10$ fs, we have that $G_{\max} = 1$ at $I_0 \approx 5 \cdot 10^{13}$ W/cm². Such intensity levels are typical of the experiments on scattering of high-power femtosecond pulses on water particles [10].

Let us consider how the field of the third harmonic (TH) is formed in a spherical particle under the effect of a femtosecond pulse. As a pulse of this duration passes through a particle, nonlinear polarization of the medium occurs at the triple frequency of every harmonic in the radiation spectrum. This polarization is the source of TH waves. If some Fourier component of the pulse spectrum is in resonance with a WG mode, then efficient nonlinear interaction between this component and the field of its TH is possible, if the TH is also the WG mode. Under such an interaction, a part of energy of the initial pulse is converted into the TH during the time the field exists in the particle. Thus, in contrast to the SRS, when the pulse itself contains components with the frequencies, whose difference is equal to the frequency of molecular vibrations, for the THG process the mode at the same frequency must be formed. To estimate the process of formation of the WG mode, we can use the approximation of the traveling wave [11]. For the intensity of TH that is generated as the pulse passes through the particle, we can write

$$I_3 = 576\pi^6 / n_a^4 \lambda_L^3 c^2 \left| \chi_{eg}^{(3)} \right|^2 I_0^3 L^2. \quad (3.47)$$

Here L is the path length along the particle surface $L \approx 2\pi a_0$; $\chi_{eg}^{(3)}$ is the component of the tensor $\hat{\chi}_e^{(3)}$ responsible for the TH generation. The estimates by Eq. (47) indicate that for particles with the radii $a_0 \sim 10$ μm the experimentally measurable signal I_3 can be achieved.

Consider the relation between the contributions due to the SRS and the THG to the distortion of the pulse spectrum. If the modes maintaining the SRS and TH overlap, then the competition is possible between these effects. To determine what effect prevails in the nonlinear interaction, we use the quasistationary approximation. In this approximation, the parameter characterizing the relation between the components of nonlinear susceptibility, which determine the contributions to the nonlinear polarization coming from the effects of forced molecular vibrations and nonlinear electronic polarizability, is as follows [8]:

$$\delta = \frac{|\text{Im} \chi_R^{(3)}|}{|\chi_{eg}^{(3)}|} = \frac{N_0}{48m} \left(\frac{\partial \alpha}{\partial Q_m} \right)^2 \frac{T_2}{\Omega_R} \left| \chi_{eg}^{(3)} \right|.$$

For water δ is equal to 0.65 [8]. This value points to the fact that in water particles the contribution coming from electronic polarizability to the process of nonlinear interaction is somewhat larger than that from the SRS.

From the above physical consideration it follows that generation of high-Q components of the light field caused by nonlinear electronic polarizability as well as of the Stokes frequencies initiated by the stimulated Raman scattering is possible for the femtosecond pulse in a microparticle. A more accurate relation between the contributions from these two processes to the general pattern can be determined from a rigorous solution of the

problem with the allowance made for the spatial and frequency interaction of the exciting and scattered fields; this solution will be considered in the future.

It is obvious that exposing the particle to a group of femtosecond pulses with the period $T_0 < \tau_r$, where τ_r is the characteristic lifetime of the mode taking part in a nonlinear interaction, we can obtain quasistationary excitation of stimulated emission. This distinguishes the pulsed interactions of a femtosecond pulse with a particle and the interaction with an extended medium, since in the latter case it is important for the pulse repetition frequency to be comparable with the frequency of molecular vibrations of the medium.

3.2.3. Two-photon fluorescence of water droplets under the exposure to intense laser radiation: experiment

The transition probability at two-photon absorption is known to be related to the radiation intensity as

$$W_2 = \sigma_2 \cdot I^2, \quad (3.48)$$

where σ_2 is the cross section of two-photon absorption.

Quantum-mechanics description of the probability of two-photon transition and the absorption cross section in the system of two real levels a and b and one virtual intermediate level n is obtained in the tensor form. For luminescent molecules, the emission cross section is measured experimentally.

If the pulse duration is longer than the lifetime of the first excited singlet state, then the fluorescence intensity is

$$I_f = \eta \sigma_2 N_0 I^2, \quad (3.49)$$

where η is the quantum yield, N_0 is the concentration of molecules.

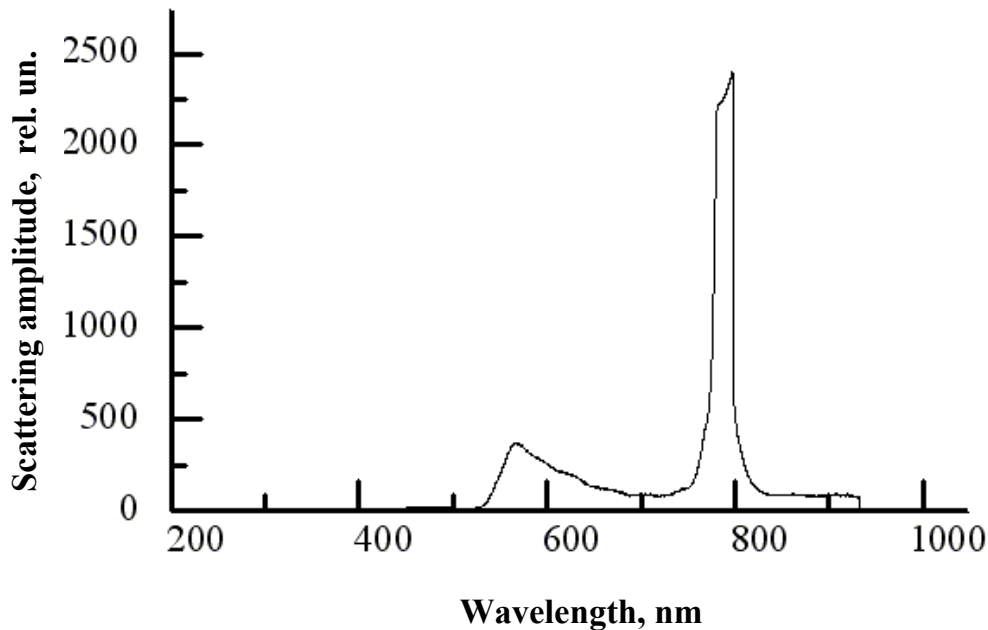


Fig. 3.9. Two-photon luminescence initiated by femtosecond pulse in dye droplets. Laser wavelength $\lambda = 820$ nm, pulse duration $\tau = 50$ fs, pulse energy $E_p = 3 - 5$ nJ.

Two-photon dye luminescence in a microparticle under the exposure to a group of femtosecond pulses is examined experimentally by us. Experiments were conducted to study two-photon induced luminescence (TPIL) in millimeter dibutylphthalate drops with Rhodamine 6G (R6G) pumped by femtosecond laser radiation with the wavelength of $0.82\ \mu\text{m}$, pulse duration of 50 fs and pulse energy of 3-5 nJ. The laser radiation was focused in the drop near-surface area. The spectra of the pump radiation and the drop glow were recorded with the resolution of 0.3 nm. The obtained emission spectrum of the R6G solution in a drop has a peak nearby $0.57\ \mu\text{m}$ and coincides with the R6G luminescence spectrum. This allows us to interpret the observed glow as two-photon induced luminescence (Fig.9).

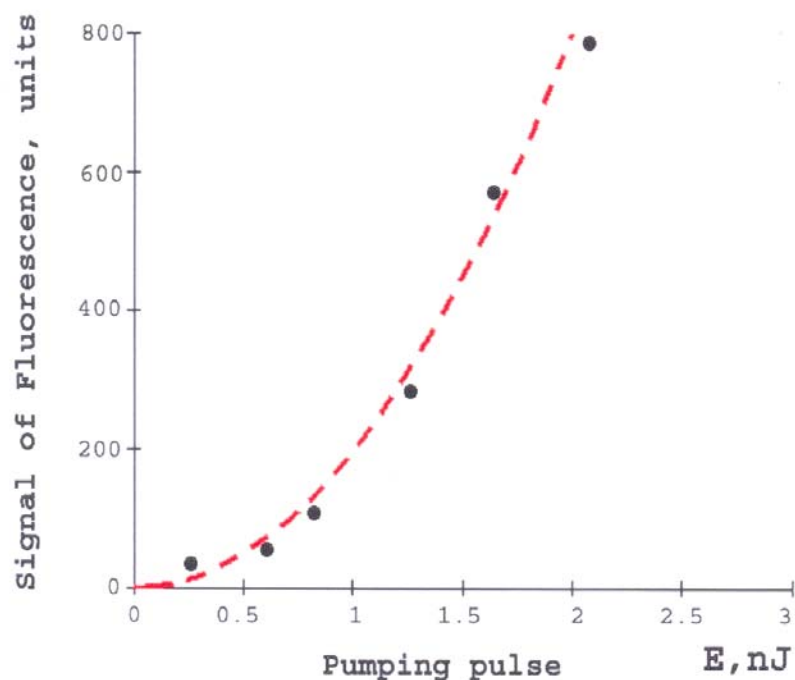


Fig. 3.10. Two-photon fluorescence of drop with R6G.

Figure 10 shows dependence of fluorescence signal energy on the femtosecond pulse energy. Clearly, it has quadratic character.

3.2.4. Second harmonic generation (SHG), third harmonic generation (THG), white light generation: overview of experimental data

In this part we present a results of detailed study of nonlinear effects in water microdroplets excited by ultrashort pulses, produced in [12] The intensities and thresholds of second-harmonic generation (SHG), third-harmonic generation (THG), white-light generation, and Raman coupled processes are compared and discussed.

The experimental setup is presented in Fig. 11. Distilled water droplets are produced by a piezoelectric-driven aerosol generator (Microdrop MD 140). The droplet radius can be tuned from 8 to $32\ \mu\text{m}$ by adjustment of the driving voltage and the pulse duration.

The femtosecond laser system consists of a Spectra-Physics Ti:sapphire laser source that produces 80-fs pulses and a Quantronix regenerative amplifier. This system provides peak powers of as much as 5.3 GW at a 1-

kHz repetition rate. The wavelength for these experiments is 810 – 820 nm, with a typical bandwidth of 10 nm. The polarization of the laser can be turned by a half-wave plate.

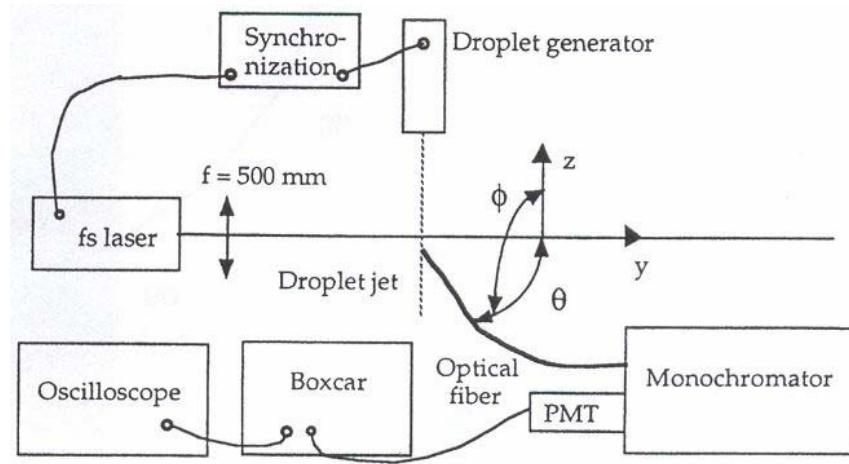


Fig. 3.11. Experimental setup for nonlinear scattering measurements of microdroplets: z , polarization direction of the laser; ϕ , angle between the scattering plane and the yz plane; θ , scattering (polar) angle toward the xz plane. PMT, photomultiplier tube.

Spectrum of nonlinear scattering from microdroplets. Figure 12 shows the wavelength dependence of the intensity emitted by a water droplet with a radius of $a = 25 \mu\text{m}$ (size parameter $k_a \approx 194$, where $k = 2\pi/\lambda$). This measurement is made at $\theta = 32^\circ$ and $\phi = 90^\circ$, with a captured solid angle of 1.8×10^{-2} sr. The laser power is $5 \times 10^{13} \text{ W cm}^{-2}$, and the pump wavelength is centered at 820 nm.

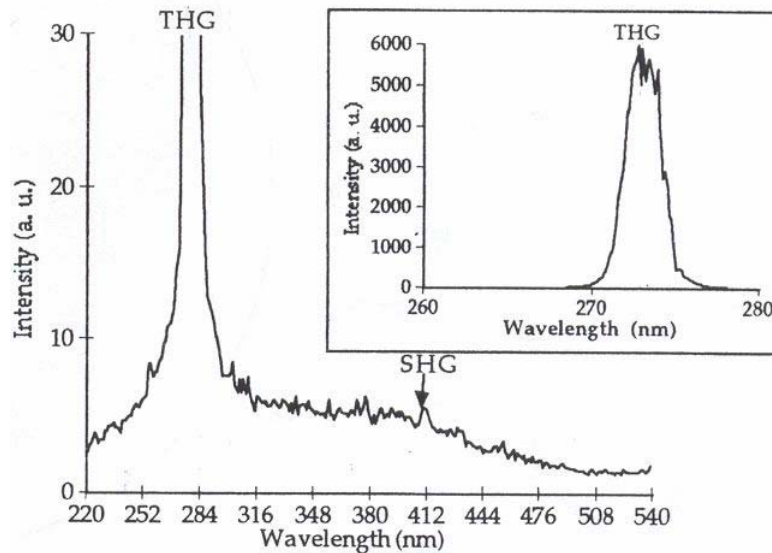


Fig. 3.12. Wavelength dependence of the intensity emitted at 32° by a water droplet with a radius of $25 \mu\text{m}$ ($k_a \sim 194$). The incident laser power is $1.7 \times 10^{13} \text{ W}\cdot\text{cm}^{-2}$, and the captured solid angle is 1.8×10^{-2} sr. Inset, third-harmonic peak at lower laser fluency ($10^{13} \text{ W}\cdot\text{cm}^{-2}$).

The main feature of the spectrum is a prominent THG peak at 273 nm. The inset shows the shape of this peak at a lower laser power ($10^{13} \text{ W}\cdot\text{cm}^{-2}$). As expected, it corresponds to the third power of the Gaussian energy distribution of the fundamental profile. In particular, its FWHM of 3 nm fits the 10-nm broad excitation

well. The power dependence of the THG light, measured for pump powers ranging from 5×10^{11} to 5×10^{13} $\text{W}\cdot\text{cm}^{-2}$, allowed us to estimate the nonlinear efficiency process $\sigma^{(3)}$, defined as

$$\frac{dP_{THG}}{d\Omega} = \sigma^{(3)} I_p^3,$$

where $dP_{THG}/d\Omega$ is the emitted THG power per solid angle unit and I_p is the incident laser power intensity. At $\theta = 32^\circ$ (close to the maximum; see below) $\sigma^{(3)}$ is estimated to be $5 \times 10^{-36} \text{ W}^{-2} \text{ cm}^6 \text{ sr}^{-1}$, whereas in backscattering ($\theta = 180^\circ$) it is found to be 1 order of magnitude lower. Our experimental threshold of observation of the process is $5 \times 10^{11} \text{ W cm}^{-2}$.

The SHG process is observable on the spectrum at 410 nm, but it is of a magnitude 1000 times weaker than that for THG. This result accounts for the good spherical shape of the droplets, because SHG is forbidden by symmetry, as in every even-order nonlinear process.

Besides SHG and THG, a very broad white-light background ($\sim 200 \text{ nm FWHM}$) is clearly observed, generated by self-phase modulation. The spectral width $\Delta\nu$ generated in these conditions can be estimated by

$$\Delta\nu = \frac{1}{\lambda} n_2 \frac{dI}{dt}, \quad (3.50)$$

where n_2 is the nonlinear refractive index of water [$4.4 \times 10^{-16} \text{ cm}^2 \text{ W}^{-1}$] and dI/dt is the temporal variation of intensity, yielding a continuum of 370-nm width per millimeter of water traversed, which is consistent with a light path in a cavity mode of a quality factor of only $7 \cdot 10^3$. Some whispering-gallery modes in liquid droplets exhibit Q factors as high as 10^8 . Although this broadband emission can be extremely attractive for spectroscopic analysis, its amplitude remains relatively low, in the best case ($\sim 340 \text{ nm}$) 3 orders of magnitude lower than for THG.

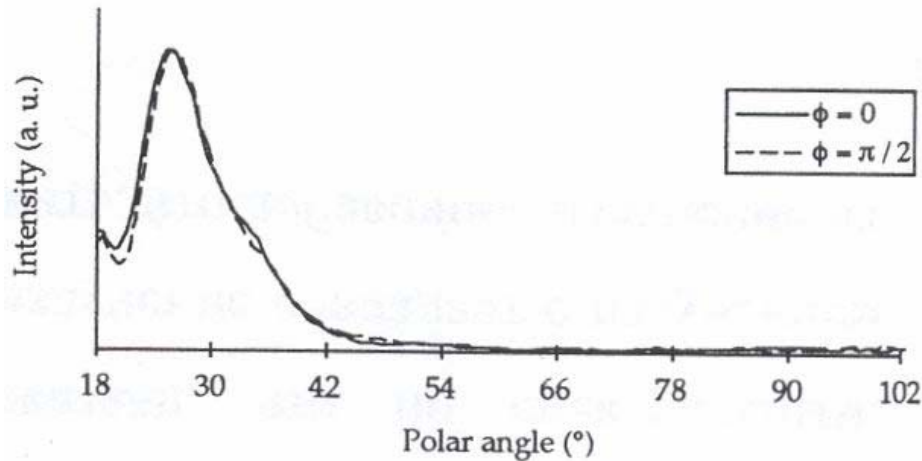


Fig. 3.13. Angular distribution of the THG from water microdroplets with radius $a \approx 10.5 \mu\text{m}$ ($k_a \approx 81$) in both azimuthal planes ($\phi = 0$ and $\phi = 90^\circ$) with the same scale Wavelength dependence of the intensity emitted at 32° by a water droplet with a radius of $25 \mu\text{m}$ ($k_a \sim 194$). The incident laser power is $1.7 \times 10^{13} \text{ W}\cdot\text{cm}^{-2}$, and the captured solid angle is $1.8 \times 10^{-2} \text{ sr}$. Inset, third-harmonic peak at lower laser fluency ($10^{13} \text{ W}\cdot\text{cm}^{-2}$).

3.3. Thresholds for laser induced optical breakdown (LIB) of aerosol medium in femtosecond time scale

The interaction of an intense laser radiation of nanosecond and picosecond duration with aerosol is accompanied by the effect of optical breakdown near aerosol particles. It has been found that in the case of absorbing particles the breakdown initially occurs in the dense vapor produced by evaporation of the particle exposed to the radiation. For weakly absorbing particles, the plasma of the optical breakdown is first produced inside the particle, and then the optical discharge propagates outside into the gas medium. The appearance of optical breakdown was observed as the glowing plasma filament in the substance and the intense acoustic signal from the region of the light beam.

In atmospheric optics the thresholds and dynamics of the development of the optical breakdown in particles are also important for evaluation of the possibility of mechanically destructing the microparticle due to dissipation of the energy stored in plasma and, in addition, in the problems of laser energy transport through the atmosphere by a series of femtosecond pulses.

The objective of this Section is theoretical calculation of the optical breakdown thresholds for transparent microparticles exposed to single laser pulses with the nano-, pico-, and femtosecond duration.

The formation of plasma in the medium upon propagation of an intense laser radiation is connected with the generation of free electrons under the effect of light field. The main physical mechanisms of photoionization of the condensed and gaseous media are the cascade (avalanche) and multiphoton ionization (MPI). The particular role of each of these ionization mechanisms in plasma formation depends on the intensity and duration of the laser pulses.

The evolution of the electron concentration in plasma is based on the system of rate equations for the concentrations of negatively n_e and positively n_p charged and neutral particles, which account for all the physical mechanisms regulating the charge balance in plasma. Under conditions of quasineutral ($n_p \approx n_e$) and quasiequilibrium plasma (thermodynamic equilibrium), only one rate equation for n_e turns out sufficient in the most cases:

$$\frac{\partial n_e}{\partial t} = \eta_{mpa} I^m + \eta_{cas} I \cdot n_e - \eta_{rec} n_e^2 - \eta_{att} n_e. \quad (3.51)$$

Here η_{mpa} , η_{cas} , η_{rec} , η_{att} are the parameters characterizing the rates of MPI, cascade ionization, recombination, and attachment of electrons, respectively; I is the intensity of laser radiation; m is the integer part of the sum $(E_i/\hbar\omega_0 + 1)$; E_i is the energy of atom ionization; ω_0 is the central frequency in the laser pulse spectrum; \hbar is the Planck constant. The first two terms in the right-hand side of Eq. (51) describe the growth of the concentration of free electrons, while the others characterize its decrease.

The rate of cascade ionization in the approximation of instantaneous energy exchange between the electron and the atom (Drude model) is expressed as follows:

$$\eta_{cas} = \frac{1}{(\omega_0 \tau_{coll})^2 + 1} \cdot \frac{\tau_{coll} \mathbf{e}^2}{n_a c \epsilon_0 m_e E_i}, \quad (3.52)$$

where m_e and \mathbf{e} are the electron mass and charge; ϵ_0 is the electric constant; n_a is the refractive index of the medium; τ_{coll} is the electron mean free time, the time between collisions.

According to MPI theory developed by L.V. Keldysh [13], an atom can be also ionized as a result of successive absorption of several radiation quanta. In this case, the bound electron receives the energy sufficient to leave the atom and form the gas of free electrons. The probability of this process is proportional to the instantaneous intensity of laser radiation to the m -th power. Unlike the cascade ionization, MPI requires rather high radiation intensity, but evolves much faster.

For calculation of the MPI rate, the equations from Ref. 4 can be used:

$$\eta_{mpa} = \frac{2\omega_0}{9\pi} \left(\frac{m'_e \omega_0}{\hbar} \right)^{3/2} \left(\frac{e^2}{16n_a c \cdot \varepsilon_0 m'_e \omega_0^2 E_i} \right)^m \exp(2m) \cdot \Phi(\xi) \quad (3.53a)$$

$$\eta_{mpa} = N_0 \omega_0 \left(\frac{E_i}{\hbar \omega_0} \right)^{3/2} \left(\frac{e^2}{4n_a c \cdot \varepsilon_0 m_e \omega_0^2 E_i} \right)^m \quad (3.53b)$$

where $m'_e \approx m_e/2$ is the reduced exciton mass; N_0 is the concentration of neutral gas molecules; $\xi = \sqrt{2(m - E_i/\hbar\omega_0)}$; $\Phi(\xi)$ is the Dawson's integral. Equation (53a) is used for condensed media, and Eq. (53b) is for the gaseous ones.

For the rate of the electron-ion recombination there are the following experimental estimates: $\eta_{rec} \approx 1.1 \cdot 10^{-12} \text{ m}^3/\text{s}$ for the atmospheric air and $\eta_{rec} \approx 2.0 \cdot 10^{-15} \text{ m}^3/\text{s}$ for water. The process of capture of free electrons by neutral molecules and formation of negative ions is described by the corresponding rate of attachment:

$$\eta_{att} = \frac{m_e \tau_{coll} \omega_0^2}{M \left[(\omega_0 \tau_{coll})^2 + 1 \right]}, \quad (3.54)$$

where M is the mass of molecule.

The evolution of the concentration n_e in pure water is shown in Fig. 14 for following parameters: laser pulse: $\lambda_0 = 800 \text{ nm}$; $I_0 = 10^{11} \text{ W/cm}^2$; $t_p = 10^{-13} \text{ s}$; medium: water, $n_{e0} = 1 \text{ m}^{-3}$; $m = 5$; $E_i = 6.5 \text{ eV}$; $\eta_{mpa} = 2.51 \cdot 10^{-48} \text{ m}^7 \cdot \text{s}^4/\text{J}^5$; $\eta_{cas} = 1.93 \cdot 10^{-4} \text{ m}^2/\text{J}$.

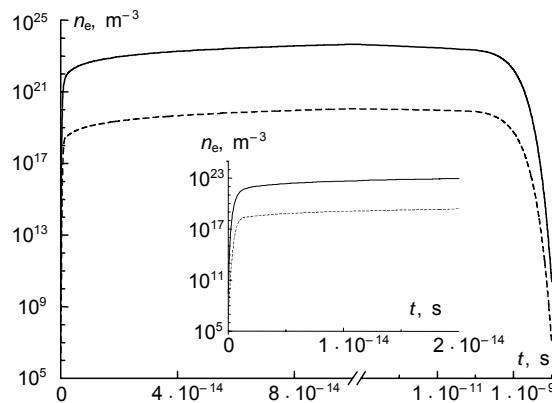


Fig. 3.14. Evolution of the concentration of free electrons in water under the exposure to a rectangular-shaped radiation pulse with the account of MPI and cascade ionization (solid curve) and at $\eta_{cas} = 0$ (dashed curve). The inserted fragment demonstrates the initial stage of the development of the electron avalanche.

It can be seen that after the quick growth the concentration of plasma electrons achieves the level of saturation, which, as will be shown below, depends on the intensity of the incident light wave. At $t > t_p$ (the time $t = t_p$ corresponds to the break of abscissa on the plot), n_e begins to decrease first as $1/t$ due to the mechanism of electron–ion recombination and then exponentially for the time $t \sim \eta_{\text{att}}^{-1}$ due to the attachment of electrons to neutral atoms.

To determine the fractions of MPI and cascade ionization in evolution of the plasma, $n_e(t)$ was calculated by Eq. (51) at $\eta_{\text{cas}} = 0$. The results of this calculation are shown by the dashed curve in Fig. 14. The level of $n_{e \text{ max}}$ turned out to be much lower in this case. This indicates that in the condensed medium (water) the role of MPI reduces to provision of seed electrons for the following development of the avalanche just due to cascade ionization.

At the same time, MPI, as known, plays a certain role in plasma formation in the gas medium at high intensity of the laser radiation. This is also confirmed by our calculations for the atmospheric air (78% N_2 and 22% O_2) at the following parameters:

$$\begin{aligned} E_i(\text{N}_2) &= 15.6 \text{ eV } (m = 11), & E_i(\text{O}_2) &= 12.5 \text{ eV } (m = 9); \\ \eta_{\text{mpa}}(\text{N}_2) &= 5.75 \cdot 10^{-165} \text{ m}^{19} \cdot \text{s}^{10}/\text{J}^{11}, & \eta_{\text{mpa}}(\text{O}_2) &= 8.21 \cdot 10^{-127} \text{ m}^{15} \cdot \text{s}^8/\text{J}^9; \\ \eta_{\text{cas}} &= 8.32 \cdot 10^{-7} \text{ m}^2/\text{J}, & \eta_{\text{rec}} &= 1.1 \cdot 10^{-13} \text{ m}^3/\text{s}, \quad \eta_{\text{att}} = 2.5 \cdot 10^7 \text{ s}^{-1}. \end{aligned}$$

In this case, to obtain the concentration of free electrons $n_{e \text{ max}} \sim 10^{24} \text{ m}^{-3}$, the radiation intensity has been increased up to $I_0 = 10^{14} \text{ W}/\text{cm}^2$.

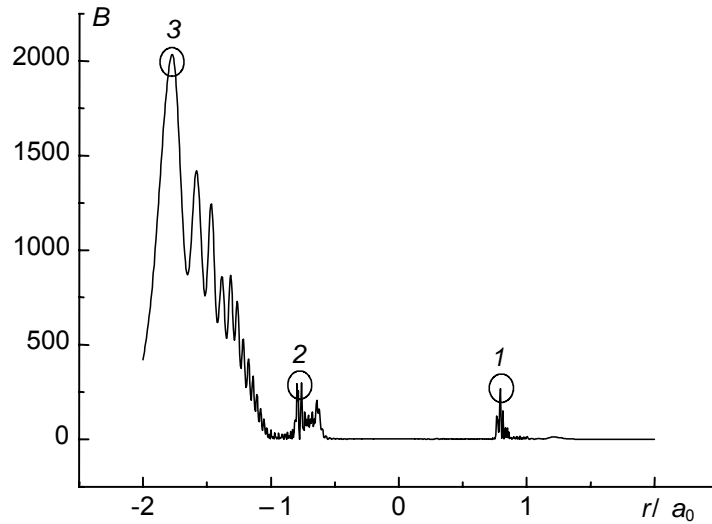


Fig. 3.15. Distribution of the factor B along the principal diameter of the water droplet (radius $a_0 = 50 \text{ }\mu\text{m}$; $n_a = 1.33$) exposed to the plane monochromatic wave with $\lambda_0 = 800 \text{ nm}$. Circles mark the intensity maxima of the optical field in the illuminated (1) and shadow (2) hemispheres and the region of geometric focus (3). The radiation is incident from the right to the left.

Consider the results of numerical simulation of the optical breakdown in the vicinity of water droplets suspended in air. The electron concentration in plasma was calculated by Eq. (51) with the account of Eqs. (52)–(54) based on the 4th-order Runge–Kutta numerical scheme. First, the model problem on the nonstationary

scattering of a plane light wave at a spherical particle was solved by the method described in Ref. 1. This yielded the dependence of the relative intensity of the optical field (inhomogeneity factor $B(\mathbf{r}; t) = I(\mathbf{r}; t)/I_0$) at some spatial points corresponding to the radiation intensity maxima in the illuminated (point 1 in Fig. 15) and the shadow (point 2) hemispheres of the droplet and in the region of the geometrical focus beyond the particle near its rear surface (point 3). Then the function $B(\mathbf{r}; t)$ was used in solution of Eq. (51).

This choice of the spatial points for the calculation of $n_e(t)$ was caused by the highest probability of formation of the plasma of the primary optical breakdown just at the places of intensity maxima of the optical field. The time dependences of the relative intensity at the points 1–3 upon scattering of the 50-fs pulse ($\lambda_0 = 800$ nm) with the Gaussian time profile are shown in Fig. 16. The zero time here corresponds to the time, when the leading edge of the pulse reaches the illuminated hemisphere of the droplet.

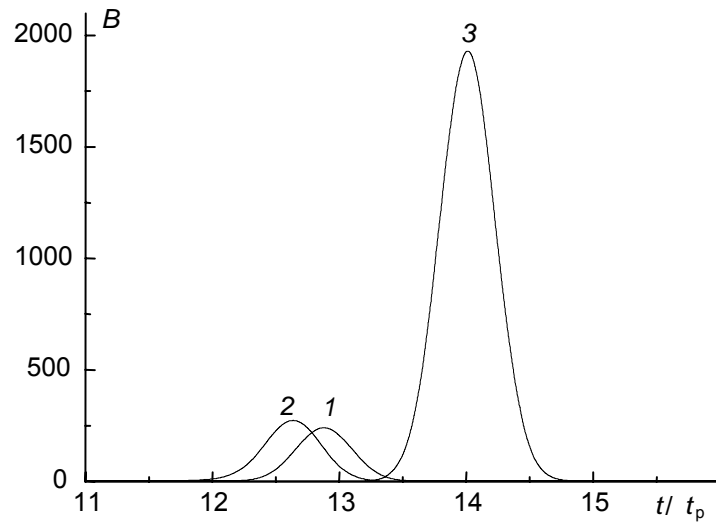


Fig. 3.16. Time dependence of the relative intensity of the optical field at the points of the front (1), rear (2), and external (3) maxima at the incidence of the radiation pulse $t_p = 50$ fs, $t_0 = 100$ fs on a water droplet ($a_0 = 50$ μm ; $n_a = 1.33$).

It follows from Fig. 16 that at the nonstationary scattering of radiation in the particle, the dependence $B(t)$ at the chosen points almost exactly copies the profile of the initial radiation pulse, is shifted in time due to the pulse propagation through the particle. First, the maximum of the internal optical field is formed in the shadow hemisphere of the particle (point 2); then, as the light wave is reflected from the rear surface of the droplet, the intensity maximum is formed in the illuminated hemisphere (point 1). Finally, the external intensity maximum is formed (point 3) near the rear surface of the particle. The maximum intensity of the optical field achievable for the exposure time (B_m) in the particle of the given size turned out practically identical at the points of the front and rear maxima: $B_m = 239.8$ (point 1) and $B_m = 272.5$ (point 2). At the same time, B_m at the point of the external field focus is almost sevenfold as high as these values: $B_m = 1930.5$ (point 3).

The evolution of the concentration of the plasma electrons at the chosen points is shown in Fig. 17. The concentration values are normalized to $n_e^{\text{th}} = 10^{26} \text{ m}^{-3}$, which are close to the experimentally measured threshold, whose excess initiates the optical breakdown in the medium [14].

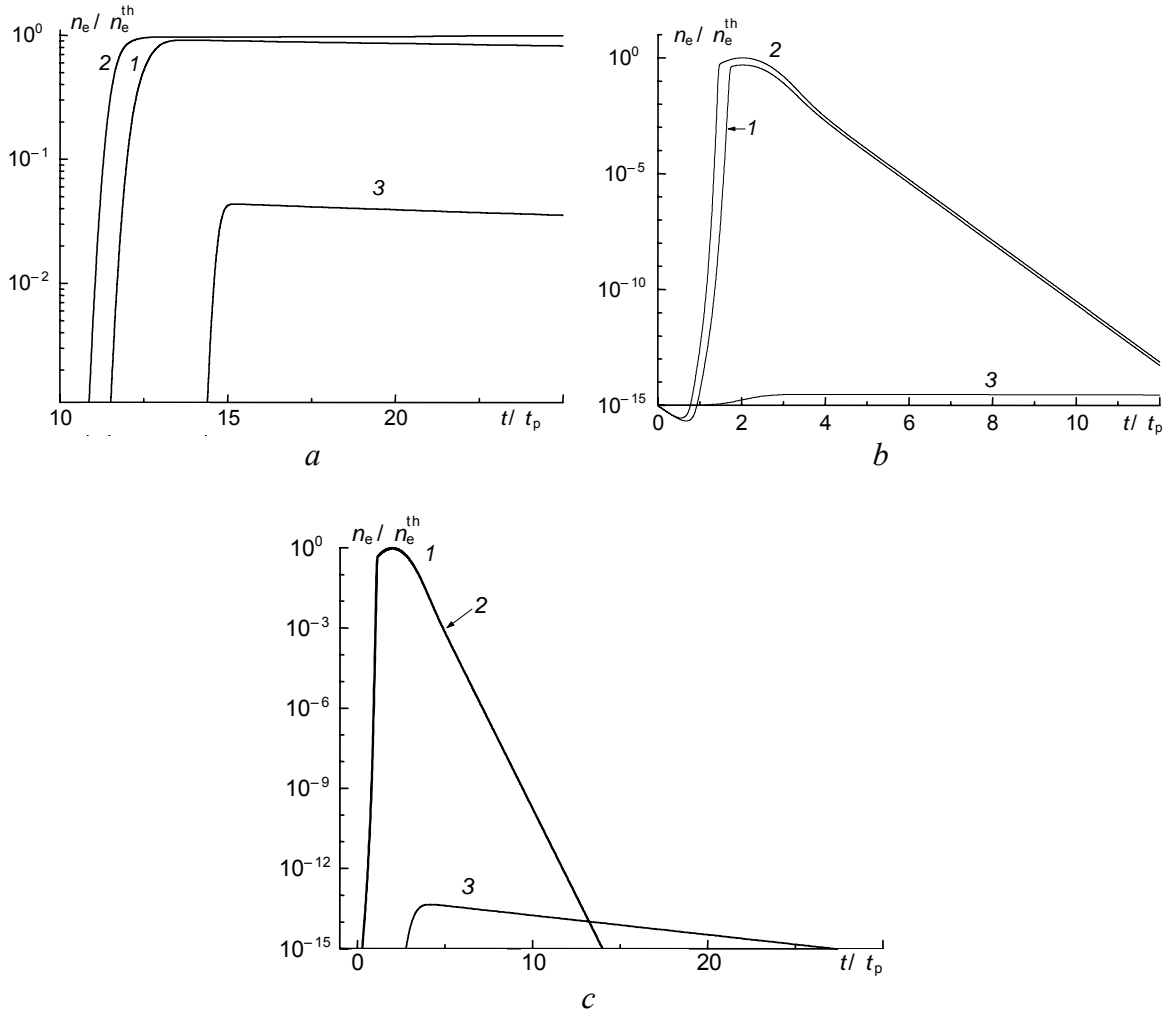


Fig. 3.17. Time dependence of the relative electron concentration in plasma n_e/n_e^{th} at the points of the front (1), rear (2), and external (3) maxima at incidence of the pulse with $\lambda_0 = 800$ nm on the water droplet ($a_0 = 50$ μm ; $n_a = 1.33$): $t_p = 50$ fs, $t_0 = 100$ fs, $I_0 = 1.18 \cdot 10^{11}$ W/cm² (a); $t_p = 1$ ps, $t_0 = 2$ ps, $I_0 = 1.1 \cdot 10^9$ W/cm² (b); $t_p = 1$ ns, $t_0 = 2$ ns, $I_0 = 7.9 \cdot 10^8$ W/cm² (c). Curves 1 and 2 coincide.

The intensity of the incident radiation corresponding to this threshold for the droplet of the radius $a_0 = 50$ μm was $I_0^{\text{th}} = 1.18 \cdot 10^{11}$ W/cm², which is two orders of magnitude higher than the threshold intensity of the breakdown of water droplets in air for nanosecond pulses of the second harmonic of a Nd : YAG laser ($\lambda_0 = 532$ nm) $I_0^{\text{th}} = 2.5 \cdot 10^9$ W/cm² and, at the same time, two orders of magnitude lower than the breakdown threshold for clean air (without aerosol) $I_0^{\text{th}} = 4\text{--}6 \cdot 10^{13}$ W/cm² ($\lambda_0 = 800$ nm). At the same time, the radiation energy density needed for initiation of the optical breakdown in the particle exposed to the pulse with $t_p = 50$ fs is only $w^{\text{th}} \sim 2$ mJ/cm², while the same parameter in water for the picosecond pulse is $w^{\text{th}} \sim 400\text{--}650$ mJ/cm².

As can be seen from Fig. 17, the threshold intensity of free electrons is achieved at the chosen irradiation intensity only at the rear focus. In the illuminated hemisphere, the values of n_e are also close to, but still lower than n_e^{th} . In this case, the maximum electron concentration n_e is only $\sim 0.05 n_e^{\text{th}}$ in the zone of the geometric focus of the incident radiation ($r/a_0 = -1.77$), in spite of the significantly higher intensity of the optical field and, consequently, the probability of breakdown here is lower.

For a comparison, Fig. 17 shows the dependence $n_e(t)$ at the incidence of the picosecond and nanosecond pulses onto the water droplet. The intensity of the incident radiation in this case was much lower: $I_0 = 1.1 \cdot 10^9$ and $7.9 \cdot 10^8$ W/cm², respectively. It should be noted that here the concentration of free electrons in the internal zones of the droplet by the time of optical breakdown is already more than 12 orders of magnitude higher than outside the particle due to, first of all, the higher rate of cascade ionization of water as compared to that of atmospheric gases.

Note that this dependence of the breakdown threshold on the laser pulse duration was discussed earlier in the theoretical paper [15] for a bulk water medium based on the numerical calculation by Eq. (51). Here we would like only to emphasize that though the presence of a microparticle decreases the threshold of the optical breakdown both inside and outside the particle, for the femtosecond radiation this effect is less pronounced than for the nano- and picosecond pulses.

Conclusions

The conclusions of our study are the following:

1. We have developed and justified a numerical approach to the study of high-power femtosecond laser pulse filamentation in the turbulent atmosphere. The nonlinear-optical model of the pulse propagation includes diffraction, material dispersion in air, instantaneous and delayed Kerr nonlinearity, generation of the laser-produced plasma, and energy losses due to multiphoton ionization of air components. Stochastic filamentation in the turbulent atmosphere is simulated by means of the Monte-Carlo on the basis of the phase screen model describing refractive index fluctuations in the atmosphere in both inertial and dissipative subranges.
2. The supercontinuum conical emission, accompanying femtosecond laser pulse filamentation, arises from the high spatio-temporal gradients of the light field intensity and the corresponding nonlinear phase. The same portions of the pulse experience high frequency shift and strong spatial divergence. Both effects are due to the fast growth of free electrons in the laser-produced plasma.
3. The simulated map of the supercontinuum sources shows that the short-wavelength components of the supercontinuum originate from the rings surrounding the high-intensity region of the pulse and from the back front of the pulse.
4. The optimum conversion efficiency to the supercontinuum in air (up to 5% of the input pulse energy) is attained if the temporal focusing length defined by the initial pulse chirp is slightly larger than the nonlinear focusing length defined by both peak power of the pulse and the geometric focusing distance.
5. The Monte-Carlo simulations have shown the increase in the number of filaments with propagation distance in atmospheric turbulence. Multiple filaments are initially formed in the central slice of the pulse with the highest peak power and move towards the pulse front with distance.
6. The calculated probability density function allows one to predict the average number of filaments produced along the atmospheric path at a certain distance from the laser system output and the variance of this number of filaments.
7. As the atmospheric turbulence strength (the structure constant) increases, the filaments are formed, on average, earlier in the propagation direction as compared to the case of weaker turbulence. With increasing inner scale of turbulence the distance to the filament formation increases. In total, the effect of the inner scale of turbulence on multiple filamentation is comparatively weak. Five time increase in the inner scale leads to, on average, 1 meter increase in the filament formation distance, that is $\sim 2\text{-}3\%$ of the typical distance of the first filament formation.
8. Under conditions of nonstationary light field diffraction on a transparent particle, the internal optical field is usually excited in a resonance way, with the eigenfrequencies of one or several high- Q resonance modes of the particle falling into the central part of the original pulse spectrum. This causes a time delay of the light in the particle and a reduction of the absolute maximum in the time dependence of the internal field intensity as compared with a stationary regime. The greatest reduction of the peak occurs at exact resonance. In this case, the decrease in the peak intensity may reach several orders of

magnitude.

9. The main difference of the repetitive scattering of pulses by a spherical microparticle from scattering by a single pulse consists in the possibility of some phasing of individual pulses in the train, when the whispering gallery modes falling within the spectral profile of the train are excited resonantly. In this case, the larger is the frequency mismatch between the natural mode and the central frequency of the incident radiation, the shorter should be the gap between the pulses.
10. At the excitation of spontaneous fluorescence in microparticles, the spectral cross section of the one-photon process for some modes can exceed the spontaneous emission cross section of the same volume of an extended medium, and this excess is proportional to the product of the factors accounting for the focusing properties of the particle and its characteristics as a dielectric microresonator. The spherical shape stipulates appearance of local maxima in the spatial intensity distribution of the pump field and the field of the secondary wave inside the microparticle and, consequently, the more efficient excitation of active molecules in the zones of local maxima as compared to the extended medium. It can be stated that just this is the main reason for asymmetry in the angular distribution of the fluorescence field from particles, which was repeatedly observed in the experiments, while the spontaneous fluorescence of a bulky substance is characterized by the isotropic angular distribution.

The signal of two-photon excited fluorescence is experimentally shown to be proportional to the square of femtosecond laser pulse energy.

11. The linear scattering of ultra-short radiation on gaseous media has no appreciable differences from its stationary analogue, therefore for estimations of integral scattering characteristics under the condition of non-stationary process it is possible to use results of the stationary theory.
12. Excitation of resonance modes of the optical field in weakly absorbing spherical particles by femtosecond-duration pulses of radiation has some peculiarities as compared with the case of long pulses (or continuous-wave radiation). These peculiarities include the decrease of the resonance intensities of the internal field, especially in the zones of field maximum (near the illuminated and shadow surfaces of the particle) and the occurrence of multimode excitation of resonance modes.
13. The efficiency of energy transfer from the incident light wave to the field of a resonance mode depends on the ratio between the spectral widths of the resonance mode being excited and of the laser pulse. The smaller is this ratio, as compared to the monochromatic wave, the less efficient is the excitation of resonances, and the intensity of the internal field in the zones of field maximum decreases.
14. The nonlinear optical effects of the SRS and THG in microparticles under the action of a high-power femtosecond pulse can occur in two stages. At the first one (transient stage), whispering-gallery modes are formed. At the second (quasistationary) stage, quasistationary generation of stimulated radiation in the Stokes and higher frequency, corresponding to the third harmonic, spectral regions is possible independent of the pulse duration.
15. The results presented indicate that the physical pattern of appearance of the optical breakdown of weakly absorbing microparticles is the same for both long and ultrashort pulses. The plasma is first formed at the rear focus inside the particle, and then, if the exposure to the radiation continues, the

optical breakdown is possible in the gas medium adjacent to the particle in the region of the geometric focus of the particle for the incident radiation. The main difference of the femtosecond mode of optical breakdown from the breakdown under the exposure to pico- and nanosecond laser pulses is in the higher ($\sim 10^2$ times) threshold intensities of the incident radiation, as well as in a more significant role of the external focal zone of the optical field diffracted at the particle in the process of formation of the primary plasma.

References

Introduction

1. Braun A., Korn G, Liu X., Du D., Squier J., Mourou G. *Opt. Lett.*, **20**, 73 (1995).
2. Nibbering E.T.J., Curley P.F., Grillon G., Prade B.S., Franco M.A., Salin F., Mysyrowicz A. *Opt. Lett.*, **21**, 62 (1996).
3. Brodeur A., Chien C.Y., Ilkov F.A., Chin S.L., Kosareva O.G., Kandidov V.P. *Opt. Lett.*, **22**, 304 (1997).
4. J. Kasparian, M. Rodriguez, G. Méjean, J. Yu, E. Salmon, H. Wille, R. Bourayou, S. Frey, Y.-B. André, A. Mysyrowicz, R. Sauerbrey, J.-P. Wolf, L. Wöste. *Science*, **301**, 61 (2003).
5. Kasparian J., Sauerbrey R., Mondelain D., Niedermeier S., Yu J., Wolf J.-P., Andre Y.-B., Franco M., Prade B., Tzortzakis S., Mysyrowicz A., Rodriguez M., Wille H., Woste L. *Opt. Lett.*, **25**, 1397 (2000).
6. Rairoux P., Schillinger H., Niedermeier S., Rodriguez M., Ronneberger F., Sauerbrey R., Stein B., Waite D., Wedekind C., Wille H., Wöste L., Ziener C. *Appl. Phys. B*, **71**, 573 (2000).
7. Q. Luo, W. Liu, and S. L. Chin. *Appl. Phys. B* **76**, 337 (2003).
8. B. La Fontaine, D. Comptois, C. Y. Chien, A. Desparois, F. G rin, G. Jarry, T. W. Johnston, J. C. Kieffer, F. Martin, R. Mawassi, H. P pin, F. A. M. Rizk, F. Vidal, C. Potvin, P. Couture, H. P. Mercure. *J. Appl. Phys.* **88**, 610-615 (2000).
9. P. Debye. *Ann. Phys. (Leipzig)*, 57–136 (1909).
10. G. Mie. *Ann. Phys. (Leipzig)*, Bd 25, H. 25, 377–445 (1908).
11. H.C. van de Hulst. *Light Scattering by Small Particles* (Dover, New York, 1981).
12. K.S. Shifrin. *Light Scattering in Turbid Medium* (Gl. Izd. Tekhniko-Teor. Lit., Moscow, Leningrad, 1951), 288 pp.
13. M. Kerker. *The Scattering of Light and Other Electromagnetic Radiation* (Academic Press, New York, 1969), 619 pp.
14. A.P. Prishivalko. *Optical and Thermal Fields inside Light Scattering Particles* (Nauka i Tekhnika, Minsk, 1983), 190 pp.
15. R. Fuchs and K.L. Kliewer. *J. Opt. Soc. Am.* **58**, No. 3, 319–330 (1968).
16. Yu.E. Geints, A.A. Zemlyanov, V.E. Zuev, A.M. Kabanov, and V.A. Pogodaev. *Nonlinear Optics of Atmospheric Aerosol* (SB RAS Publishing House, Novosibirsk, 1999), 260 pp.
17. A.N. Kalinenko and S.D. Tvorogov. *Zh. Prikl. Spektrosk.* **XX**, No. 1, 140–145 (1968).
18. D.Q. Chowdhury, S.C. Hill, and P.W. Barber. *J. Opt. Soc. Am. B* **9**, No. 8, 1364–1373 (1992).
19. K.S. Shifrin and I.G. Zolotov. *Appl. Opt.* **34**, No. 3, 552–558 (1995).
20. A.A. Zemlyanov and Yu.E. Geints. *Atmos. Oceanic Opt.* **14**, No. 5, 316–325 (2001).
21. K.S. Yee. *IEEE Trans. Antennas and Propag.* **Ap-14**, No. 3, 302–307 (1966).
22. P. Yang, K.N. Liou, M.I. Mishchenko, and Bo-Cai Gao. *Appl. Opt.* **39**, No. 21, 3727–3737 (2000).
23. Chew H., McNulty P.J., Kerker M. *Phys. Rev.* **13**, 396-404 (1976).

24. Schweiger G., Lange S. *JOSA B*. **13**, No. 9, 1864-1872 (1996).
25. Hill S.C., Pan Y., Holler S., Chang R.K. *Phys. Rev. Lett.* **85**, № 1, 54-57 (2000).
26. Zemlyanov A.A., Geints Yu.E., Panina E.K. *Proc. SPIE*. **5396**, 205-211 (2003).
27. G. Schweiger. *J. Aerosol Sci.* **21**, No. 4, 483-509 (1990).
28. W.P. Acker, D.H. Leach, and R.K. Chang. *Opt. Lett.* **14**, No. 8, 402-404 (1989).
29. D.H. Leach, R.K. Chang, W.P. Acker, and S.C. Hill. *J. Opt. Soc. Am. B*. **10**, No. 1, 34-45 (1993).
30. J. Kasparian, B. Kramer, T. Leisner, P. Rairoux, V. Boutou, B. Vezin, and J.P. Wolf. *J. Opt. Soc. Am. B* **15**, No. 7, 1918-1922 (1998).
31. Y.-X. Yan, E.B. Gamble, and K.A. Nelson. *J. Chem. Phys.* **85**, No. 11, 5391-5399 (1985).
32. A.M. Weiner, D.E. Leaird, G.P. Wiederrecht, and K.A. Nelson. *J. Opt. Soc. Am. B* **8**, No. 6, 1264-1275 (1991).
33. E.M. Belenov, A.V. Nazarkin, and I.P. Prokopovich. *Pis'ma Zh. Eksp. Teor. Fiz.* **55**, No. 4, 223-227 (1992).
34. A. Nazarkin and G. Korn. *Phys. Rev. A* **58**, No. 1, R61-R64 (1998).

Chapter 1,2

1. Braun A., Korn G, Liu X., Du D., Squier J., Mourou G. *Opt. Lett.*, **20**, 73 (1995).
2. Nibbering E.T.J., Curley P.F., Grillon G., Prade B.S., Franco M.A., Salin F., Mysyrowicz A. *Opt. Lett.*, **21**, 62 (1996).
3. Brodeur A., Chien C.Y., Ilkov F.A., Chin S.L., Kosareva O.G., Kandidov V.P. *Opt. Lett.*, **22**, 304 (1997).
4. J. Kasparian, M. Rodriguez, G. Méjean, J. Yu, E. Salmon, H. Wille, R. Bourayou, S. Frey, Y.-B. André, A. Mysyrowicz, R. Sauerbrey, J.-P. Wolf, L. Wöste, *Science*, **301**, 61 (2003).
5. Kasparian J., Sauerbrey R., Mondelain D., Niedermeier S., Yu J., Wolf J.-P., Andre Y.-B., Franco M., Prade B., Tzortzakis S., Mysyrowicz A., Rodriguez M., Wille H., Woste L. *Opt. Lett.*, **25**, 1397 (2000).
6. Rairoux P., Schillinger H., Niedermeier S., Rodriguez M., Ronneberger F., Sauerbrey R., Stein B., Waite D., Wedekind C., Wille H., Wöste L., Ziener C. *Appl. Phys. B*, **71**, 573 (2000).
7. Q. Luo, W. Liu, and S. L. Chin, *Appl. Phys. B* **76**, 337 (2003).
8. B. La Fontaine, D. Comptois, C. Y. Chien, A. Desparois, F. G rin, G. Jarry, T. W. Johnston, J. C. Kieffer, F. Martin, R. Mawassi, H. P pin, F. A. M. Rizk, F. Vidal, C. Potvin, P. Couture, H. P. Mercure, *J. Appl. Phys.* **88**, 610-615 (2000).
9. Kosareva O.G., Kandidov V.P., Brodeur A., Chien C.Y., Chin S.L. *Opt. Lett.*, **22**, 1332 (1997).
10. M. Mlejnek, E.M. Wright, J.V. Moloney: *Opt. Lett.* **23**, 382 (1998)
11. Y. R. Shen, *The Principles of Nonlinear Optics* (J. Wiley & Sons, New York, 1984).
12. I.S. Golubtsov, O.G. Kosareva: *Journal of Optical Technology* **69**, 462 (2002).
13. S.A. Akmanov, V.A. Vysloukh, A.S. Chirkin, *Optics of Femtosecond Laser Pulses* (American Institute of Physics, New York, NY, 1992).
14. T. Brabec, F. Krausz: *Phys. Rev. Lett.* **78**, 3282 (1997).

15. A.M. Perelomov, V.S. Popov, M.V. Terent'ev: Sov. Phys. JETP 23, 924 (1966).
16. A. Talebpour, J. Yang, S.L. Chin: Opt. Comm., **163**, 29 (1999).
17. S.L. Chin, A. Talebpour, J. Yang, S. Petit, V.P. Kandidov, O.G. Kosareva, M.P. Tamarov, Appl. Phys. B **74**, 67–76 (2002).
18. A. Ishimaru: *Wave Propagation and Scattering in Random Media*, V.2 (Acad. Press, New York, San Francisco, London 1978)
19. B.J. Herman, L.A. Strugala: Proc. SPIE **1221**, 183, (1990).
20. R.G. Lane, A. Glindemann, J.C. Dainty: Waves in Random Media **2**, 209 (1992).
21. E.M. Johanson, D.T. Gavel: Proc. SPIE **2200**, 372, (1994).
22. . S.S. Chesnokov, V.P. Kandidov, M.P. Tamarov, S.A. Shlenov: Proc. SPIE **3432**, 14, (1998).
23. I.S. Golubtsov, V.P. Kandidov, O.G. Kosareva, Atmos. Oceanic. Opt. **14**, 966 (2001).
24. J.H. Marburger: Prog. Quant. Electron. **4**, 35, (1975)

Chapter 3

1. A.A. Zemlyanov and Yu.E. Geints. *Atmos. Ocean. Opt.* **15**, 619-627, (2002).
2. A.A. Zemlyanov and Yu.E. Geints. *Atmos. Ocean. Opt.* **16**, 898-902, (2003).
3. A.A. Zemlyanov and Yu.E. Geints. *Atmos. Ocean. Opt.* **14**, 316-325, (2001).
4. K.S. Shifrin. *Light scattering in turbid medium* (Gos. Izdat. Techniko-Teor. Lit., Moscow – Leningrad, 1951), 288 pp.
5. A.A. Zemlyanov and Yu.E. Geints. *Atmos. Ocean. Opt.* **15**, 1088-1094, (2001).
6. S.C. Hill, Y. Pan, S. Holler, R.K. Chang. *Phys. Rev. Lett.* **85**, 54-57, (2000).
7. C.A. Akhmanov, V.A. Vysloukh, and A.S. Chirkin. *Optics of femtosecond pulses* (Nauka, Moscow, 1988), 312 pp.
8. C.A. Akhmanov and N.I. Korotaev. *Methods of nonlinear optics in spectroscopy of light scattering* (Nauka, Moscow, 1981), 544 pp.
9. A.A. Zemlyanov and Yu.E. Geints. *Atmos. Ocean. Opt.* **12**, 895-904, (1999).
10. Yu.E. Geints, A.A. Zemlyanov, V.E. Zuev, A.M. Kabanov, and V.A. Pogodaev. *Nonlinear Optics of Atmospheric Aerosol* (SB RAS Publishing House, Novosibirsk, 1999), 260 pp.
11. G. Rogers. *Nonlinear parametric processes in liquids and gases* [Russian translation] (Mir, Moscow, 1987), 510 pp.
12. J. Kasparian, B. Kramer, T. Leisner, P. Rairoux, V. Boutou, B. Vezin, and J.P. Wolf. *J. Opt. Soc. Am. B* **15**, 1918-1922 (1998).
13. L.V. Keldysh. *Zh. Eksp. Teor. Fiz.* **47**, 1945–1956 (1964).
14. C.H. Fan, J. Sun, and J.P. Longtin. *J. Appl. Phys.* **91**, 2530–2536 (2002).
15. A. Vogel, J. Noack, K. Nahen, D. Theisen, S. Busch, U. Parlitz, D.X. Hammer, G.D. Noojin, B.A. Rockwell, and R. Birngruber. *Appl. Phys. B* **68**, 271–280 (1999).

Head of the Project



Alexander A. Zemlyanov